To the Graduate Council:

I am submitting herewith a dissertation written by Jeffrey Scott Thompson entitled "Photoelectron Spectroscopy of Negative Ions: Energy– and Angle–Resolved Measurements." I have examined the final copy of this document for form and content and recommend that it be accepted in partial fulfillment of the requirements for the degree of Doctor of Philosophy, with a major in Physics.

David J. Pegg, Major Professor

We have read this dissertation
and recommend its acceptance:

Edward D Hayes

Robert Norman Compton

Carrol R. Bingham

Accepted for the Council:

Vice Provost
and Dean of the Graduate School

PHOTOELECTRON SPECTROSCOPY OF NEGATIVE IONS: ENERGY- AND ANGLE-RESOLVED MEASUREMENTS

A Dissertation

Presented for the

Doctor of Philosophy

Degree

The University of Tennessee, Knoxville

Jeffrey Scott Thompson

May 1989

Copyright ©Jeffrey Scott Thompson, 1989

All rights reserved

ACKNOWLEDGMENTS

Many people have contributed to the success of this project. My research advisor, Dr. David Pegg, has been directly responsible for my training as a scientist. He has encouraged me and been patient during the difficult times, and let his exuberance show when the experiment worked. I deeply appreciate his help and friendship.

Drs. Gerald Alton and Robert Compton were associated with this project before my tenure began. I have relied heavily on their physical insight and technical expertise. I owe them a great deal.

When I began working on this project, Dr. Thomas Kvale was a postdoctoral fellow in charge of the operation and maintenance of the accelerator. I followed Tom as he worked and asked a tremendous number of what I now know to be ridiculous questions. Tom always took the time to explain what I didn't understand and for that I am extremely grateful.

The work described in this thesis was performed at the Oak Ridge National Laboratory. I would like to thank the members of the Atomic Physics Section and the Physics Division for the enlightening interactions. The Oak Ridge National Laboratory is a splendid place to work and learn.

I also wish to thank my parents, Elton and Roselyn Thompson. They have always encouraged my interest in science. Without them, I would not have been able to explore the realms of science, nor could I have attained my educational goals.

Finally, I would like to express my gratitude to my wife, Michele. I have spent numerous hours in the laboratory that we had planned to spend together. Her love and support have been instrumental in the completion of this project.

Funding from the Department of Energy, Division of Chemical Sciences, is gratefully acknowledged.

ABSTRACT

A crossed laser–negative ion beams apparatus has been used to investigate both Ca^- and He^- ions. The fast negative ion beam was perpendicularly crossed with a photon beam from a flashlamp–pumped dye laser. Photoelectrons ejected in the direction of the ion beam were collected and energy analyzed by an electrostatic electron spectrometer. The resolved electron peaks in the spectra corresponded to photodetachment processes that left the residual atoms in either their ground state or excited states.

Experimental evidence is presented to show that Ca^- is a stable ion and is formed in the $(4s^24p)\ ^2P$ state. This result represents the first report of a stable negative ion for a Group IIA element. The structure of Ca^- was determined by means of photoelectron detachment spectroscopy. Kinematic effects associated with a fast moving ion beam were exploited, in a novel way, in these experiments. The electron affinity of Ca was measured to be 0.043 ± 0.007 eV, which is in good agreement with recent calculations.

Energy– and angle–resolved spectroscopy measurements have been used to study, for the first time, the spectral dependence of the angular distributions of electrons photodetached from a beam of He^- ions. Photoelectron angular distributions were measured by varying the angle between the electric field vector of the linearly polarized laser beam and the fixed collection direction. In the spectral range of the measurements, 1.775 – 2.456 eV, photodetachment into either the $He(1s2s)\ ^3S$ + e or $He(1s2p)\ ^3P$ + e continua is allowed. These competing channels were resolved and the spectral dependence of the angular distributions were measured for each case. The $He(1s2s)\ ^3S$ exit channel produced a spectral dependence that could be explained, using an independent electron description, by interferences between the outgoing s– and d–waves. The shape of the spectral dependence for the $He(1s2p)\ ^3P$ exit channel could not, however, be explained by

an independent electron model. Correlation is seen to affect the electron emission processes. Various final state interaction models are discussed to account for the observed spectral dependence.

TABLE OF CONTENTS

1 INTRODUCTION 1

2 THEORY 7
- 2.1 Introduction . . . 7
- 2.2 Photon–Negative Ion Collisions . . . 8
- 2.3 Negative Ion Structure . . . 17

3 EXPERIMENTAL APPARATUS 20
- 3.1 Introduction . . . 20
- 3.2 Ion Source and Ion Beam Line . . . 21
- 3.3 Laser and Optics . . . 27
- 3.4 Electron Energy Analyzer . . . 31
- 3.5 Electronics and Data Acquisition System . . . 37

4 ELECTRON AFFINITY OF THE CALCIUM ATOM 44
- 4.1 Introduction . . . 44
- 4.2 Photoelectron Spectroscopy . . . 46
- 4.3 Experimental Results . . . 49
  - 4.3.1 Data Analysis . . . 49
  - 4.3.2 Error Analysis . . . 52
- 4.4 Conclusion . . . 54

5 PHOTODETACHMENT OF He^-: ANGULAR DISTRIBUTION OF PHOTOELECTRONS 58
- 5.1 Introduction . . . 58
- 5.2 Energy– and Angle–Resolved Measurements . . . 62
- 5.3 Photoelectron Asymmetry Parameters . . . 67
  - 5.3.1 Introduction . . . 67
  - 5.3.2 Asymmetry Parameter for the He(^{3}S) Exit Channel . . . 69
  - 5.3.3 Asymmetry Parameter for the He(^{3}P) Exit Channel . . . 69
- 5.4 Error Analysis . . . 75
- 5.5 Conclusion . . . 76

BIBLIOGRAPHY 78

APPENDIX **85**
A.1 Introduction 86
A.2 Transformation of Kinetic Energies and Angles 86
A.3 Transformation of Solid Angle 89
A.4 Rotation of Angular Distributions 90
A.5 Relativistic and Recoil Effects 92

VITA **93**

LIST OF FIGURES

1.1 Electron affinities of the elements in the first half of the periodic table 3

2.1 Photoelectron angular distributions for β = 2,0,-1 15

3.1 Ion source schematic; 1- housing endcap(Ta), 2- ion source housing(Mo), 3- exit aperture(W), 4- filament(W), 5- filament cup(Ta), 6- anode(Ta), 7- oven(BN), 8- heater wire(Mo), 9- insulator(BN) . 22
3.2 Schematic of the ion accelerator 24
3.3 Schematic of the crossed–beams apparatus 30
3.4 Schematic of a spherical–sector analyzer 32
3.5 Spherical–sector electron spectrometer 35
3.6 Electronics and data acquisition system 40
3.7 Timing diagram for the synchronous detection of photoelectrons . 42

4.1 A typical kinetic energy spectrum of photoelectrons produced in the process, $Ca^- + h\nu \longrightarrow Ca + e^-$. Peaks 1 and 2 are associated with the photodetachment channel leaving the Ca atom in the ^3P state. Peak 3 corresponds to the photodetachment channel leaving the Ca atom in the ^1S state. 48
4.2 Energy level diagram of the lowest lying states of Ca and Ca^- . . . 55

5.1 Partial energy level diagram of He and He^- 61
5.2 A typical kinetic energy spectrum of electrons photodetached from a beam of He^- ions. Peaks 1 and 2 are associated with the photodetachment channel that leaves the He atom in the ^3P state. Peak 3 corresponds to the photodetachment channel that leaves the He atom in the ^3S state. 64
5.3 Angular dependence of the photoelectron yield for the ^3P exit channel 66
5.4 Spectral dependence of the asymmetry parameter for electrons photodetached from He^- via the ^3S exit channel 70
5.5 Spectral dependence of the asymmetry parameter for electrons photodetached from He^- via the ^3P exit channel 72

A.1 Transformation from laboratory rest frame to ion rest frame 87

A.2 The effect of kinematics on photoelectron angular distributions . . 91

CHAPTER 1

INTRODUCTION

Negative ions play an important role in a number of areas of physics and chemistry involving ionized gases. In astrophysics, for example, photodetachment and its inverse process, radiative electron attachment, play an important role in determining the solar continuous spectrum. It has been shown that absorption of photons by H^- in the solar photosphere determines the spectral distribution in the optical region [1]. Photon absorption by C^- may be important in determining the opacity of hydrogen–deficient carbon stars [2]. Such transitions in He^- are also considered to be a major source of the opacity of some white dwarf stars [3]. Low energy negative ion collisions with atoms and molecules leading to rearrangement and association can play an important role in interstellar space and in planetary atmospheres. Negative ion chemistry, for example, plays an important role in the D region of the Earth's ionosophere [4]. Negative ions are also used in many applications. In fusion research, for example, negative ions are used to produce intense atomic beams for injection heating of tokamak plasmas. Negative ions are also necessary for the operation of electrostatic accelerators based on the tandem principle.

A stable negative ion is produced when an electron attaches itself to an atom in its ground state. The formation of such an ion involves a delicate balance between attractive forces supplied by the nucleus and interelectronic repulsive forces. A neutral atom does not, of course, exert any net Coulomb force on an extra electron. Shielding of the nucleus by the atomic electrons and correlation effects between the relative motions and spins of the electrons both play important roles in determining whether a stable negative ion will exist. The deeper the extra electron penetrates the atomic electron cloud, the less effectively the atomic electrons shield

the nucleus. Furthermore, the attached electron tends to polarize the atomic electron cloud to some degree, subjecting the extra electron to attractive higher–multipole forces. Radial and angular correlation increase the spread of the electron charge distribution of the negative ion, as they tend to keep the electrons further apart. As a result, interelectronic repulsion is reduced.

The stability of negative ions is determined by the weak and short–ranged force that binds the additional electron. This force arises from polarization and exchange effects and it falls off with distance in an approximately fifth–power law [4]. The short ranged nature of the binding force limits the number of bound states that can be accommodated in the shallow potential well to, typically, one. The simple structure of negative ions means that only bound–free transitions can be studied following photoabsorption. The characteristically small binding energies associated with the attached electrons make negative ions rather fragile.

The electron affinity of an atom is defined as the difference in the total energies of the atomic parent state and the negative ion state. The electron affinity of an atom is numerically equivalent to the binding energy of the least tightly bound electron of a negative ion. By this definition, a positive electron affinity indicates a bound negative ion state.

Although the net force binding the additional electron is weak and short–ranged, over 80% of the naturally occurring elements are able, under appropriate conditions, to form a stable negative ion. Fig. 1.1 shows the electron affinities of elements in the first half of the periodic table that form stable negative ions. The open circles represent experimentally determined electron affinities, and the dots represent electron affinities that have been determined by calculations. With the notable exception of the halogens, the electron affinity of most elements is seen to be equal to or less than 1 eV.

Another class of negative ions are metastable ions. In this case, electrons

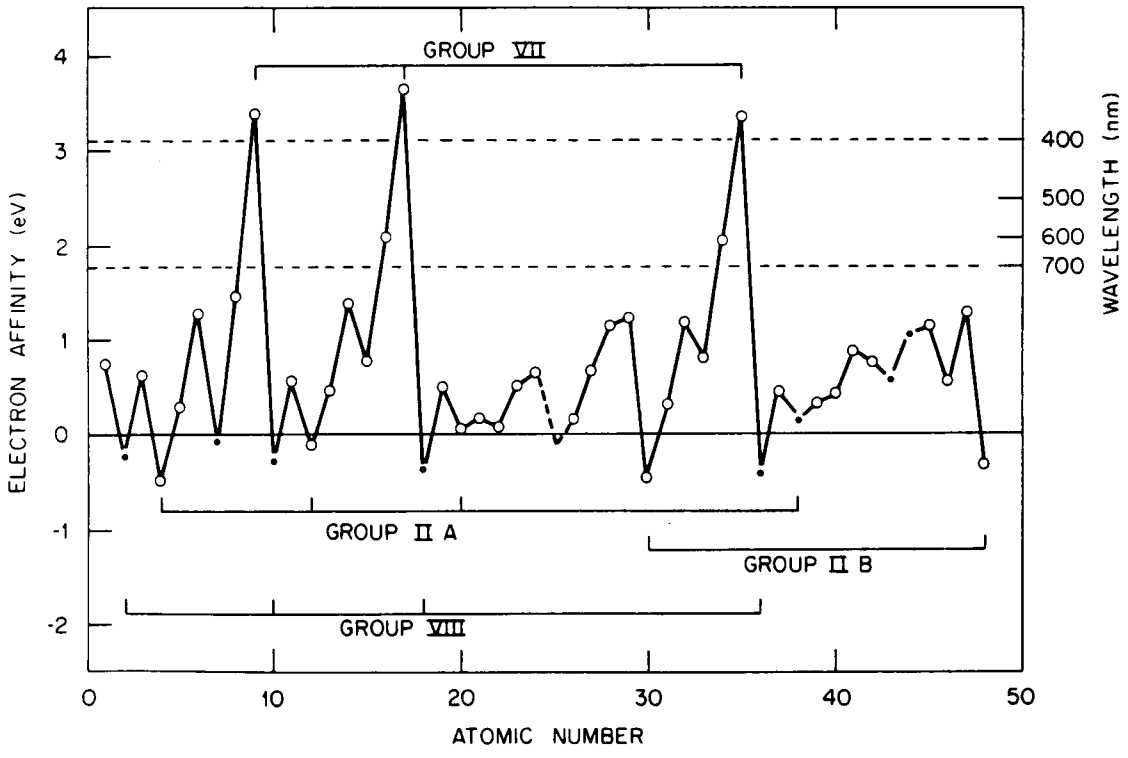


Figure 1.1: Electron affinities of the elements in the first half of the periodic table

attach themselves to atoms in metastable excited states. The states are metastable against allowed autodetachment and radiative decay. Eventually such metastable states relax via forbidden autodetachment processes. The lifetimes of these states are typically $\sim 10^{-6}$ to $\sim 10^{-4}$ s, sufficiently long to be studied and to be of practical value.

To study negative ions, the experimental techniques must be designed to take account of the fragility of negative ions. It is difficult, for example, to produce negative ions in sufficient quantities for experiments because of their high probability of being destroyed in collisions. The atomic processes that are involved in the production of these ions must generally compete with the more probable processes for destroying them. Ion beam sources are typically used in negative ion studies. This type of source provides a reasonable density of ions in a tenuous environment that reduces the probability of their unwanted destruction by collisions.

Two bound–free spectroscopic techniques have been developed to study negative ions; photodetachment spectroscopy and photoelectron detachment spectroscopy. In photodetachment spectroscopy, the number of atoms or electrons produced is observed as a function of the incident photon energy. In particular, measuring the threshold energy for the onset of production of either the atom or the electron provides an accurate way of determining the electron affinities of atoms. In 1954, Branscomb and Fite [5] introduced the crossed ion–photon beams technique for studying the spectral dependence of the cross section for photodetachment of H^- using a non–laser light source. The shape of the cross section curve was monitored as a function of the photon energy. Since then the technique has been improved by the use of laser beams as the photon source [6].

In the second technique, photoelectron detachment spectroscopy, a measurement is made of the kinetic energy of the electrons emitted during the pho-

todetachment process. This technique is based on the energy balance equation used by Einstein [7] to explain the photoelectric effect. In a bound–free transition, the kinetic energy of the photoelectron is equal to the photon energy less the energy required to reach the final state of the atom. Thus, if the photon wavelength is well known, measurement of the electron's kinetic energy provides a method of determining the binding energy of the electron in the negative ion and hence the electron affinity of the atom. Photoelectron energy spectra from negative ions are usually quite simple and easy to interpret because negative ions typically have only one bound state. In 1966, Brehm, Gusinow and Hall [8] reported the first application of the photoelectron detachment spectroscopy technique for the measurement of an electron affinity. Their measurement on a beam of He^- ions was made using a crossed laser–ion beams apparatus. The majority of electron affinities that have been measured were determined using this same technique (see Ref. [6]). The photoelectron detachment spectroscopy technique was also employed in the measurements reported in this thesis. A fast negative ion beam was crossed perpendicularly with the photon beam from a flashlamp–pumped dye laser. Spectra were obtained of the yield of photoelectrons as a function of their kinetic energy using an electrostatic electron energy spectrometer. Results of two different types of experiments are reported.

The electron affinity of the Ca atom was measured, and the structure of Ca^- was determined by means of photoelectron detachment spectroscopy. This result represents the first report of a stable negative ion of the Group IIA elements. The kinematic effects associated with a slow electron ejected from an ion in a fast moving beam were exploited to determine the electron affinity of Ca. The structure of Ca^- was determined from the relative spacings of the peaks in the photoelectron spectra.

In the second set of measurements reported in this thesis, the spectral

dependence of the angular distribution of electrons ejected in the photodetachment of He^- is reported. A beam of metastable He^- ions was crossed perpendicularly with a linearly polarized photon beam from a flashlamp–pumped dye laser. The spectral range employed was from 1.775 to 2.456 eV. The energy–resolved electrons resulted from the competing photodetachment processes that left the He atom in either of two energetically accessible states. The shape of the emission pattern of photoelectrons at a particular photon energy was obtained by recording spectra as a function of the angle between the polarization vector of the laser light and the fixed collection direction of the photoelectrons.

CHAPTER 2

THEORY

2.1 Introduction

The interaction of electromagnetic radiation with matter has been intensively studied both experimentally and theoretically. Of particular interest for this thesis is the process whereby matter absorbs a single quantum of electromagnetic radiation with sufficient energy to eject an electron via a bound–free transition. Hertz's [9] century–old investigation of the photoelectric effect, a process in which electrons are ejected when light illuminates a metal, is the first recorded study of this phenomenon. Einstein [7] later explained this effect by suggesting that electromagnetic energy is quantized. The photoelectron is ejected by the absorption of a quantum of radiation energy. These important studies were instrumental in the development of quantum mechanics.

In the case of atomic systems in the gaseous phase, the photoelectric effect is usually called photoionization. Similarly, the process involving negative ions as the target is known as photodetachment. Photodetachment of a negative ion A^- can be written as

$$A^- + h\nu \longrightarrow A + e^- \tag{2.1}$$

where the products of the bound–free transition are a free electron and a neutral atom A, which may or may not be in an excited state.

The difference between the total energy of the parent atomic state and the total energy of the negative ionic state is defined as the electron affinity. The electron affinity of an atom is numerically equal and opposite in sign to the binding energy of the least tightly bound electron in the negative ion. The electron affinity, E_a, the photon energy, $E_\gamma = \hbar\omega$, and the kinetic energy of the photodetached

electron, E, are related to one another via the well known Einstein energy balance equation

$$E = E_\gamma - E_a. \tag{2.2}$$

The advent of lasers and sensitive electron spectrometers made possible precise measurements of the kinetic energies of photoelectrons, which, in turn, led to the determination of electron affinities using Eq. 2.2.

The collisional properties of the photodetachment interaction can also be studied by photoelectron detachment spectroscopy. Measurements can be made of important quantities such as cross sections for photodetachment, branching ratios for leaving the residual atom in different states and angular distributions of photoelectrons.

2.2 Photon–Negative Ion Collisions

The purpose of this section is to outline the theory of the process of photodetachment. The cross section for photodetachment from the simplest negative ion, H^-, is used as an example. This problem helps develop an understanding of the salient features of the more general theory. Review articles by Burke [10] and Cooper and Zare [11] discuss this subject in depth. An equation describing the differential cross section for the absorption of a photon and the subsequent emission of an electron can be derived using a non–relativistic, semi–classical approach (the electromagnetic field is treated classically).

The Hamiltonian describing the interaction of an electron in a static potential with a classical electromagnetic field can, in atomic units, be written as,

$$H = \frac{1}{2}[\vec{P} + \frac{1}{c}\vec{A}(\vec{r},t)]^2 + V(r)] \tag{2.3}$$

where $\vec{A}$ is the vector potential of the electromagnetic field. This Hamiltonian contains the stationary kinetic and potential energy operators, H_o, plus a time–

dependent perturbation, H′,

$$H = H_o + H'. \tag{2.4}$$

If no sources of the electromagnetic field are present, the Hamiltonian can be reduced, in the Coulomb gauge ($\vec{\nabla} \cdot \vec{A}(\vec{r}, t) = 0$), to the two parts,

$$H_o = \frac{1}{2}\vec{P}^2 + V(r) \tag{2.5}$$

$$H' = \frac{1}{c}\vec{A}(\vec{r}, t) \cdot \vec{P}. \tag{2.6}$$

The $\vec{A} \cdot \vec{A}$ term, which is second order in 1/c, has been neglected since it corresponds to the absorption of two photons, a process which is highly improbable under the conditions of the present experiment.

The time–dependent perturbation term in the Hamiltonian couples the electron to the electromagnetic field. To study the dynamics of this interaction, time–dependent perturbation theory is applied. Fermi's Golden Rule states that if a system is initially in the state $|i\rangle$ and the perturbation is turned on at a time t=0, the probability per unit time of a transition to a final state, $|f\rangle$, is

$$W_{if} = 2\pi \mid M_{if} \mid^2 \rho_f \delta(E) \tag{2.7}$$

where $M_{if} = \langle f | H' | i \rangle$ is the transition matrix element of the interaction and ρ_f is the density of final states. In the case of photodetachment, the density of final states contains a delta function, $\delta(E)$, which constrains the energy of the ejected electron to be

$$E = E_\gamma - E_a. \tag{2.8}$$

To evaluate W_{if} for the photodetachment of H^-, expressions for M_{if} and ρ_f must be derived.

The vector potential, $\vec{A}$, in the transition matrix element can, in the Coulomb gauge, be described as a traveling wave of electromagnetic radiation [12],

i.e.

$$\vec{A}(\vec{r},t) = 2\vec{A}_o \cos(\vec{k}\cdot\vec{r} - \omega t) \tag{2.9}$$

or in complex notation

$$\vec{A}(\vec{r},t) = \vec{A}_o^*(\vec{r})e^{i\omega t} + \vec{A}_o(\vec{r})e^{-i\omega t}. \tag{2.10}$$

The first term on the right hand side of Eq. 2.10 corresponds to emission of a photon and is not physically meaningful in a description of photodetachment. The second term is retained since it is associated with the absorption of a photon. The spatial part of the vector potential can be written as

$$\vec{A}_o(\vec{r}) = \hat{\varepsilon} A_o e^{i\vec{k}\cdot\vec{r}}, \tag{2.11}$$

here $\hat{\varepsilon}$ is a unit vector characterizing the polarization of the electromagnetic field. The form of the vector potential under the above conditions becomes

$$\vec{A}(\vec{r},t) = \hat{\varepsilon} A_o e^{i(\vec{k}\cdot\vec{r}-\omega t)}. \tag{2.12}$$

The initial state, $|i\rangle$, for the photodetachment of H^- is a wavefunction describing the bound state of the two–electron system. The initial–state wavefunction represents a definite state of angular momentum and parity. Perkeris [13], for example, has used a sophisticated variational calculation to obtain a very accurate approximate wavefunction for the ground state of the H^- ion.

The final–state wavefunction, $|f\rangle$, corresponds to a liberated electron moving in the potential field generated by the residual H atom. It should have the asymptotic form of a plane wave plus an incoming spherical wave when the photoelectron is far from the atom. The final state is analogous to the wavefunction used in electron–hydrogen scattering calculations. The wavefunction for the scattered electron does not have a unique orbital angular momentum and therefore is represented as a sum of partial waves, each with a unique value of angular

momentum, ℓ. A suitable final–state wavefunction is given by Smith [14] as

$$|f\rangle = \frac{4\pi}{\sqrt{V}} \sum_{\ell,m} i^{\ell} e^{i\delta_{\ell}} Y_{\ell m}(\hat{k}) G_{k\ell m}(\vec{r}) \tag{2.13}$$

where $G_{k\ell m}(\vec{r})$ is the radial wavefunction for the liberated electron, $\hat{k}$ is the unit vector along the ejection direction, δ_{ℓ} is the phase shift of the ℓth partial scattered wave, and V is the normalization volume for the momentum eigenfunction of the free electron.

The transition matrix element now becomes

$$M_{if} = \frac{A_o}{c} \langle f | \, e^{i\vec{k}\cdot\vec{r}} \hat{\varepsilon} \cdot \vec{P} \, | i \rangle \, . \tag{2.14}$$

If the wavelength of the incident electromagnetic radiation is large compared with the atomic dimensions, the exponential in the operator of Eq. 2.14 can be expanded in a Taylor series about r = 0. Under these conditions, the calculation of M_{if} is sufficiently accurate in the dipole approximation, which retains only the first terms, i.e. unity, in the expansion of $e^{i\vec{k}\cdot\vec{r}}$. The matrix element of Eq. 2.14 can now be cast in the "velocity" form of the electric dipole approximation

$$M_{if} = \frac{A_o \hat{\varepsilon}}{c} \cdot \langle f | \, \vec{P} \, | i \rangle \, . \tag{2.15}$$

Using Heisenberg's equations of motion, one can also write the above matrix element in the "length" form

$$M_{if} = \frac{-i(E_f - E_i) A_o \hat{\varepsilon}}{c} \cdot \langle f | \, \vec{r} \, | i \rangle \tag{2.16}$$

or

$$M_{if} = \frac{-i(E_f - E_i) A_o \hat{\varepsilon}}{c} \cdot \vec{r}_{if} \tag{2.17}$$

where the energy difference $E_f - E_i$ is equal to the energy of the incident photon, $E_{\gamma} = \hbar\omega$, and $\vec{r}_{if}$ is used as a shorthand notation for the radial matrix element $\langle f | \, \vec{r} \, | i \rangle$.

If the final states of the free electron can be approximated by plane waves at distances far from the region of the interaction [12], the density of final states can be written as

$$\rho_f(\vec{k}) = \frac{V}{(2\pi)^3}. \tag{2.18}$$

In terms of the kinetic energy of the liberated electron, E, Eq. 2.18 is

$$\rho_f(E) = \frac{V}{(2\pi)^3}\sqrt{2E}, \tag{2.19}$$

where the electron of momentum $\vec{k}$ is ejected into a solid angle $d\Omega$.

Substituting Equations 2.17 and 2.19 into Eq. 2.7 gives the transition rate into the final state as

$$W_{if} = \frac{\sqrt{2E}E_\gamma^2 \mid A_o \mid^2}{c^2(2\pi)^2} \mid \hat{\varepsilon} \cdot \vec{r}_{if} \mid^2 . \tag{2.20}$$

This transition rate is valid for the semiclassical description of absorption of a single photon using the "length" form of the electric dipole approximation.

For the classical description of the incident electromagnetic radiation, the intensity is equal to the Poynting vector averaged over one period of oscillation [15], i.e.

$$I = \frac{1}{8\pi}(\vec{E}^2 + \vec{B}^2). \tag{2.21}$$

The electric field, $\vec{E}$, and magnetic field, $\vec{B}$, can be expressed in terms of the vector potential using Maxwell's equations. Substituting their values into Eq. 2.21 gives

$$I = \frac{E_\gamma^2}{2\pi c^2} \mid A_o \mid^2 . \tag{2.22}$$

The number of photons per unit area per unit time, Φ, is

$$\Phi = I/E_\gamma \tag{2.23}$$

so that

$$\mid A_o \mid^2 = \frac{2\pi c^2}{E_\gamma}\Phi. \tag{2.24}$$

The differential cross section for detachment per photon is defined as the transition rate per ion per unit solid angle divided by the incident photon flux, i.e.

$$\frac{d\sigma}{d\Omega} = \frac{W_{if}}{\Phi}. \tag{2.25}$$

Substituting Equations 2.20 and 2.24 into Eq. 2.25 yields

$$\frac{d\sigma}{d\Omega} = \frac{\sqrt{2E}E_\gamma}{2\pi} \mid \hat{\varepsilon} \cdot \vec{r}_{if} \mid^2 . \tag{2.26}$$

In the above equation, the wavefunctions in the matrix element can be separated into radial and angular components. A more general form of Eq. 2.26 can be written as

$$\frac{d\sigma}{d\Omega} = \frac{\sigma}{4\pi} f(\theta, \phi) \tag{2.27}$$

where $f(\theta, \phi)$ describes the angular correlation between the incident photon and outgoing electron, θ and ϕ are the polar and azimuthal angles, respectively, and σ is the total (integrated) cross section defined such that

$$\sigma = \int \frac{d\sigma}{d\Omega} d\Omega. \tag{2.28}$$

The total cross section depends on the radial parts of the matrix element while the function $f(\theta, \phi)$ completely characterizes the angular part of the matrix element.

If the target negative ions are unpolarized (i.e., the magnetic sublevels are equally populated) and the incident light is linearly polarized, the unit vector $\hat{\varepsilon}$ can be used as the quantization axis for the problem. Defining this axis as the z–axis ensures that the problem has azimuthal symmetry about the polarization vector of the radiation. This eliminates the ϕ dependence of the angular distribution. Eq. 2.27 is therefore reduced to

$$\frac{d\sigma}{d\Omega} = \frac{\sigma}{4\pi} f(\theta). \tag{2.29}$$

Yang [16] has shown that if the target ion is unpolarized the angular distribution, in the center of mass, of outgoing particles created in a collision is a

sum of even polynomials of $\cos\theta$ with a maximum exponent not greater than 2L. The angle, θ, is the angle between the quantization axis and the direction of the outgoing particle, and L is the angular momentum of the incident particle. The spin of a linearly polarized photon is one, therefore the angular factor, $f(\theta)$, can be cast in the form

$$f(\theta) = a + b\cos^2\theta. \tag{2.30}$$

A form that is also commonly used in angular distribution studies is

$$f(\theta) = 1 + \beta P_2(\cos\theta) \tag{2.31}$$

where $P_2(\cos\theta)$ is the second–order Legendre polynomial, $\frac{1}{2}(3\cos^2\theta - 1)$ and β is an asymmetry (anisotropy) parameter. The asymmetry parameter, β, completely characterizes the shape of the emission pattern of the photoelectrons.

The differential cross section and total cross section must be non–negative numbers, and this restricts the value of β to $-1 \leq \beta \leq 2$ (see Fig. 2.1). For the case $\beta = 2$, the angular distribution is peaked about the polarization vector of the light in a $\cos^2\theta$ distribution. In the case $\beta = -1$, the distribution is proportional to $\sin^2\theta$, or peaked in a plane at right angles to the polarization vector. The distribution is isotropic for the case $\beta = 0$.

Cooper and Zare [11] have formulated an expression for the asymmetry parameter associated with one–electron systems using a non–relativistic, independent particle model. When an electron is photoejected from an initial state with orbital angular momentum ℓ, and the outgoing electron is represented by two partial waves of angular momentum $\ell' = \ell \pm 1$, β can be written as

$$\beta = \frac{\ell(\ell-1)D_{\ell-1}^2 + (\ell+1)(\ell+2)D_{\ell+1}^2 - 6\ell(\ell+1)D_{\ell+1}D_{\ell-1}\cos(\delta_{\ell+1} - \delta_{\ell-1})}{(2\ell+1)[\ell D_{\ell-1}^2 + (\ell+1)D_{\ell+1}^2]} \tag{2.32}$$

where D_ℓ is the radial dipole integral,

$$D_\ell = \int_0^\infty r R_i G_{k\ell} dr. \tag{2.33}$$

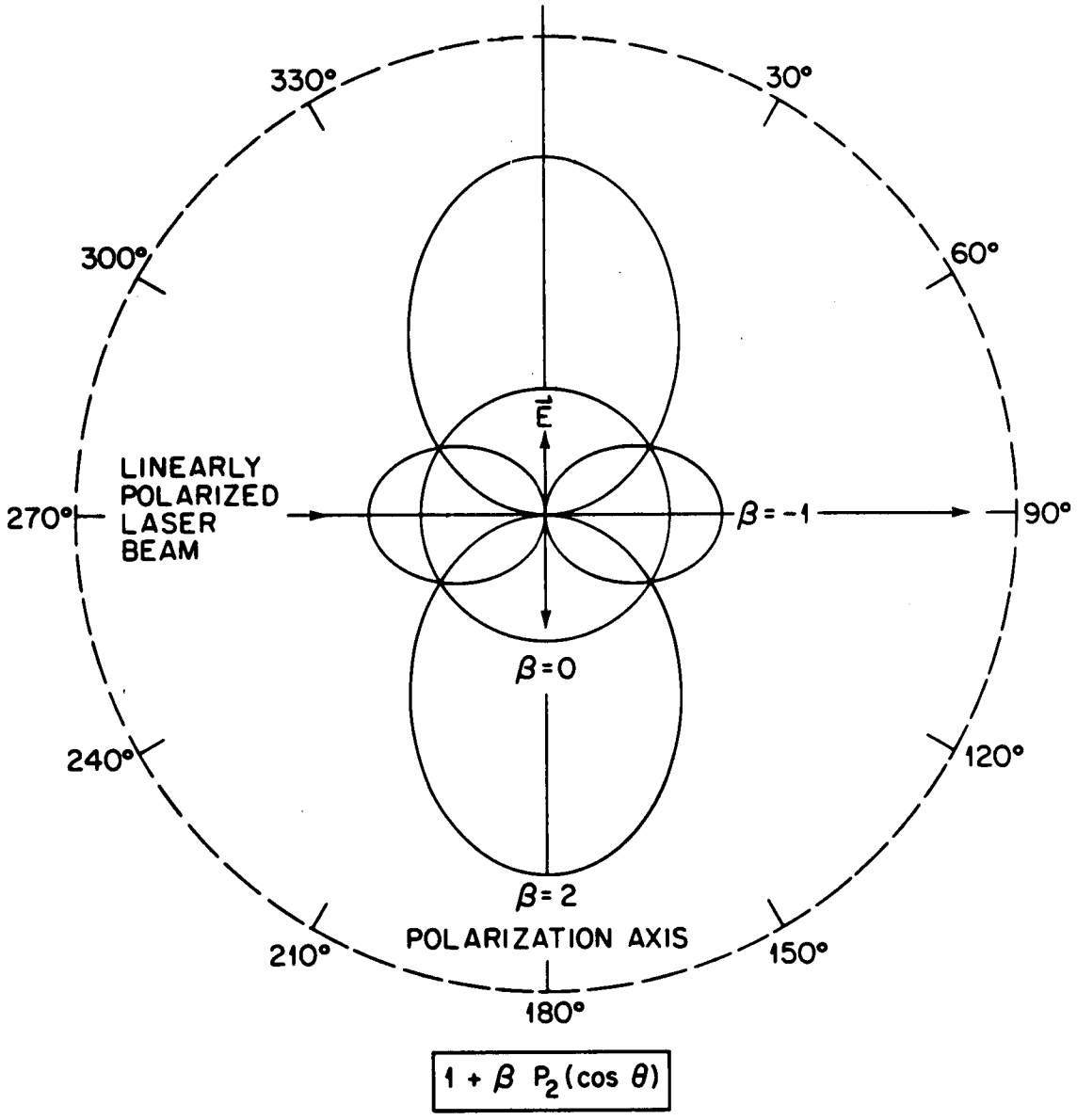


Figure 2.1: Photoelectron angular distributions for β = 2,0,-1

Here $G_{k\ell}$ is the radial wavefunction representing the outgoing electron in the final state, and R_i is the radial wavefunction of the initial state.

The asymmetry parameter, as formulated using an independent electron model (see Eq. 2.32), reduces to $\beta = 2$ for the photoejection of an s–orbital electron ($\ell = 0$). In this case, the angular distribution of electrons is proportional to $\cos^2\theta$ for all photon energies. When electrons are photoejected from orbitals other than s–orbitals, two competing channels ($\ell \pm 1$) are always present and β will depend on the interference of the partial waves associated with these channels. The asymmetry parameter will then be sensitive to both the relative magnitudes of the dipole integrals and the phase differences for the two channels and will, in general, vary as a function of the incident photon energy.

The form of β, expressed in Eq. 2.32, remains the same for many–electron systems that can be described by L–S coupling. Cooper and Zare [11] have shown that L–S coupling introduces multiplicative factors that are the same for all terms, therefore the measured angular distributions will be the same as those predicted by the independent electron theory.

If the effects of electron correlation in the initial state are included, however, the angular distribution will change. An effective asymmetry parameter for a system whose initial state is multiconfigurational can be calculated by weighting the individual one–electron configuration asymmetry parameters by the square of the configurational mixing coefficients. The effective angular distribution will depend therefore on the amounts of the configuration mixing.

The theory of angular momentum transfer was applied to the atomic photoemission process by Fano and Dill [17]. They showed that the Cooper–Zare independent electron model only treats the first step of the photoemission process – the absorption of a photon and the subsequent ejection of an electron. The Cooper–Zare model neglects the interaction of the outgoing electron with

the residual core. The dynamic coupling of the orbital angular momenta of the outgoing electron and the residual core has been shown (see Ref. [18]) to lead to spectrally–dependent deviations of the angular distribution from the predictions of the independent electron model. Dill [19] has also shown that angular distributions of photoelectrons will depart markedly from the Cooper–Zare model in the vicinity of a resonance. These final state effects are the result of anisotropic interactions between the liberated electron and the residual core. The resulting exchange of angular momentum will, in general, cause angular distributions to be quite different than those predicted by the Cooper–Zare model.

In order to account for these post–collisional effects, Dill et al. [18] have applied this angular momentum formalism to the calculation of the differential cross section for photoejection of electrons. The model uses electron–atom scattering amplitudes to describe the post–collision interactions that occur during the photodetachment process. In this model, the form of the angular correlation factor, as expressed in Eq. 2.31, does not change, but β can no longer be represented by the relatively simple expression of Eq. 2.32.

2.3 Negative Ion Structure

In order for an electron to attach itself to an atom, it must experience a net attractive force. There exists a delicate balance between forces supplied by the attractive nuclear charge and the repulsive electronic cloud associated with the atomic electrons. The net force binding the additional electron in a negative ion is weak and falls off with distance in an approximately inverse fifth–power law [4]. It arises from polarization and exchange effects. This weak and short–ranged force is responsible for the characteristically small binding energy of the attached electron, which makes negative ions fragile, and the limited number (usually one) of bound states of negative ions.

The electron affinity (E_a) of an atom is defined as the difference in the total energy of the atomic parent state (A) and the negative ion state (A^-), i.e.

$$E_a = E_{tot}(A) - E_{tot}(A^-). \tag{2.34}$$

A positive value of the electron affinity indicates a bound negative ion state. The electron affinity is a small difference between two large total energies. This makes electron affinities difficult to calculate since correlation effects become important.

The total electronic energy of an atomic or ionic level [20] can be written as

$$E_{tot} = E_{HF} + E_{cor} + \delta \tag{2.35}$$

where E_{HF} corresponds to the Hartree–Fock (central field) energy, E_{cor} is the correlation energy, which is a measure of the non–central part of the interelectronic force in a many–electron system and δ includes small corrections for mass polarization, relativistic and radiative effects. The Hartree–Fock energy is by far the largest term in Eq. 2.35, but the correlation energy is often found to be the term that plays the most decisive role in determining the electron affinity of an atom. The correlation effects, which take account of the relative motion and spins of the electrons, tend to reduce the mean interelectronic repulsion between the attached electron and the atomic electrons. The reduction of this repulsive force is often the major source of stability in negative ions [4]. Hartree–Fock energies are presently relatively easy to calculate and so the determination of an electron affinity essentially depends on how well one can calculate the difference in correlation energies, $E_{cor}(A) - E_{cor}(A^-)$.

The importance of correlation can be demonstrated using the simplest negative ion, H^-, as an example. Being a three–body problem, there is not an analytic solution for the total energy of H^-. The system is sufficiently simple, however, that a sophisticated variational calculation [13], which employs elaborate

correlated wavefunctions, can be used. The total energy of the ground state of the H^- ion calculated using a Hartree–Fock model fails to result in stability. The electron affinity in this case is -0.328 eV [21]. The correlation energy in H^- amounts to -1.083 eV [21] and this is sufficient to stabilize the negative ion. In this case, the correlation energy is 7.5% of the total energy and, in effect, it is responsible for "gluing" the additional electron to the ground state of the H atom.

The H^- ion is unique in that it represents the only case where the electron affinity of an atom is better known theoretically than experimentally. The calculated value is known to an accuracy of 3 parts in 10^7 while the experimental value is only accurate to a few parts in 10^4. The theoretically determined electron affinities of He [22] and Li [23] are presently known to about the same accuracy as the experimental results. In the case of negative ions with more than four electrons, experimental determinations of the electron affinities are presently more accurate than calculations [6]. The difficulty in determining the amount of correlation that needs to be included in calculations for many–electron systems makes it difficult for theory to challenge experimental accuracy.

CHAPTER 3

EXPERIMENTAL APPARATUS

3.1 Introduction

The basic apparatus described in this chapter has been previously used to study the production of negative ions via two sequential electron capture collisions in lithium vapor [24], and the structure of metastable negative ions by autodetachment spectroscopy [25],[26],[27]. Modifications have been made so that the negative ion beam can be crossed with a photon beam from a laser. The crossed–beams apparatus makes it possible to investigate both the structure of negative ions and their collisional properties in radiation fields.

The procedure of the experiment can be described as follows. Positive ions are extracted from a hollow cathode ion source and post accelerated to a desired kinetic energy. The ion beam is momentum analyzed by a 90° bending magnet and focused through a lithium vapor charge exchange cell, where a small fraction of the positive ions sequentially capture two electrons and form negative ions. Just after the entrance into the experimental chamber, the positive and negative ions are deflected by $\pm 10°$ with respect to the incident beam direction by a set of electrostatic plates. The separated negative ion beam is then perpendicularly crossed with a photon beam from a flashlamp–pumped dye laser just prior to the entrance of a 160° electrostatic spherical–sector electron energy analyzer. By ramping the voltage on the entrance aperture of the analyzer, a spectrum is obtained that contains information about the energies and yields of the photoelectrons produced in the photon–ion collisions. Signals proportional to the instantaneous negative ion and laser beam intensities are also collected for the purpose of normalizing the photoelectron yields. The experimental chamber is

surrounded by Helmholtz coils to minimize stray magnetic fields in the interaction region and at the site of the electron spectrometer.

3.2 Ion Source and Ion Beam Line

The ion source used in these experiments is a modified version of a Danfysik Model 911A hot filament, hollow cathode, universal positive ion source. A schematic of the ion source is shown in Fig. 3.1. The changes made in the ion source design enhanced the ion beam output intensity and simplified the operating maintenance requirements.

The ion source housing has been modified so that the filament is compressed by a threaded housing endcap, making the disassembly and reassembly of the ion source (to replace oxidized filaments) much simpler. The original oven on this ion source has been replaced with a larger oven made of boron nitride (BN). Increasing the interior volume of the oven permits a larger amount of a solid source material to be used and hence longer ion source operating times. The exterior of the oven has grooves for a heater wire (typically 0.102 cm diameter molybdenum) so that a solid source material can be heated by passing a current through the wire. The oven temperature is controlled by the heater wire current which can be optimized for the maximum output current for a particular source material.

The positive ions in the source are created by a simple physical process. Electrons are emitted from the 0.102 cm diameter tungsten filament when a current flows from the filament cup through the filament to the molybdenum ion source housing which is at "ground" potential. Applying a positive voltage to the anode causes the electrons to be accelerated toward the anode. The electrons collide with and ionize some of the atoms or molecules in the support gas that is leaked through a variable–rate leak valve. The gas flows from the oven through the ion source. When the ion density becomes high enough in the region between the anode and

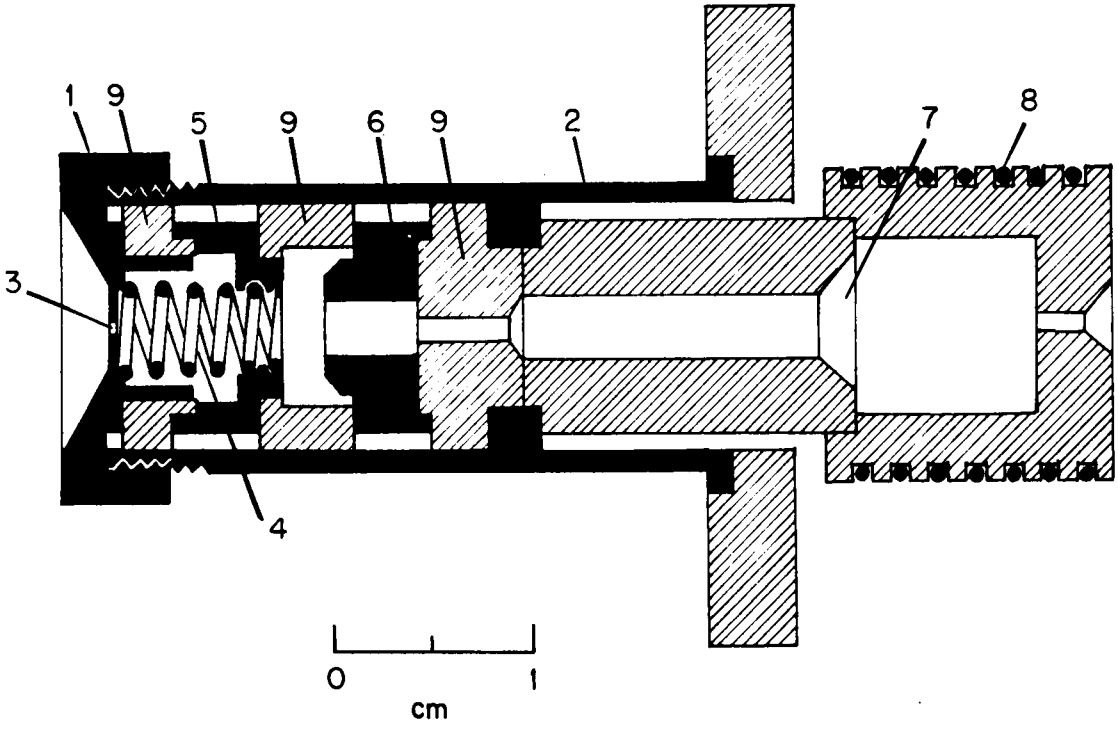


Figure 3.1: Ion source schematic; 1- housing endcap(Ta), 2- ion source housing(Mo), 3- exit aperture(W), 4- filament(W), 5- filament cup(Ta), 6- anode(Ta), 7- oven(BN), 8- heater wire(Mo), 9- insulator(BN)

filament cup a plasma–like discharge strikes between them. This discharge is the source of positive ions for the ion beam.

Under normal operating conditions helium is used as the support gas, but argon, hydrogen, deuterium and nitrogen have been used with similar results. For maximum ion beam current, the support gas is leaked into the source at a rate which raises the pressure of the ion source chamber to $\sim 2 \times 10^{-5}$ Torr. With a current of 30 A through the filament and a potential of 120 V on the anode, a total positive beam current of ~ 20 μA can be extracted from the ion source.

The positive ions are accelerated to form a beam by "floating" the ion source to a total positive acceleration voltage of 20 to 120 kV and, in effect, pushing the ions out of the source toward ground potential. The acceleration starts when the voltage is dropped by 10 kV across the 1.30 cm gap between the ion source and the extraction electrode (refer to Fig. 3.2). An Einzel lens is used to focus the beam through the post–acceleration stage, where the acceleration voltage (total acceleration voltage minus the extraction voltage) is resistively dropped through thirteen stages to ground by a linearly–graded accelerator tube. After exiting the acceleration stage, the total positive ion beam current extracted from the ion source can be monitored on a Faraday cup that can be inserted into the path of the beam.

The beam is then momentum–analyzed by a 90° bending magnet. The magnet has a mass–energy product of thirty–six and has a high enough resolution to easily separate mass differences of one atomic mass unit. Another Faraday cup can be inserted after the beam has been momentum selected so that the ion source parameters can be set to maximize the beam current of the ion to be studied.

A set of magnetic deflectors and an Einzel lens are used to steer and focus the positive ion beam through the lithium vapor charge exchange cell. The charge exchange cell is a commercially designed and manufactured unit [28] which has

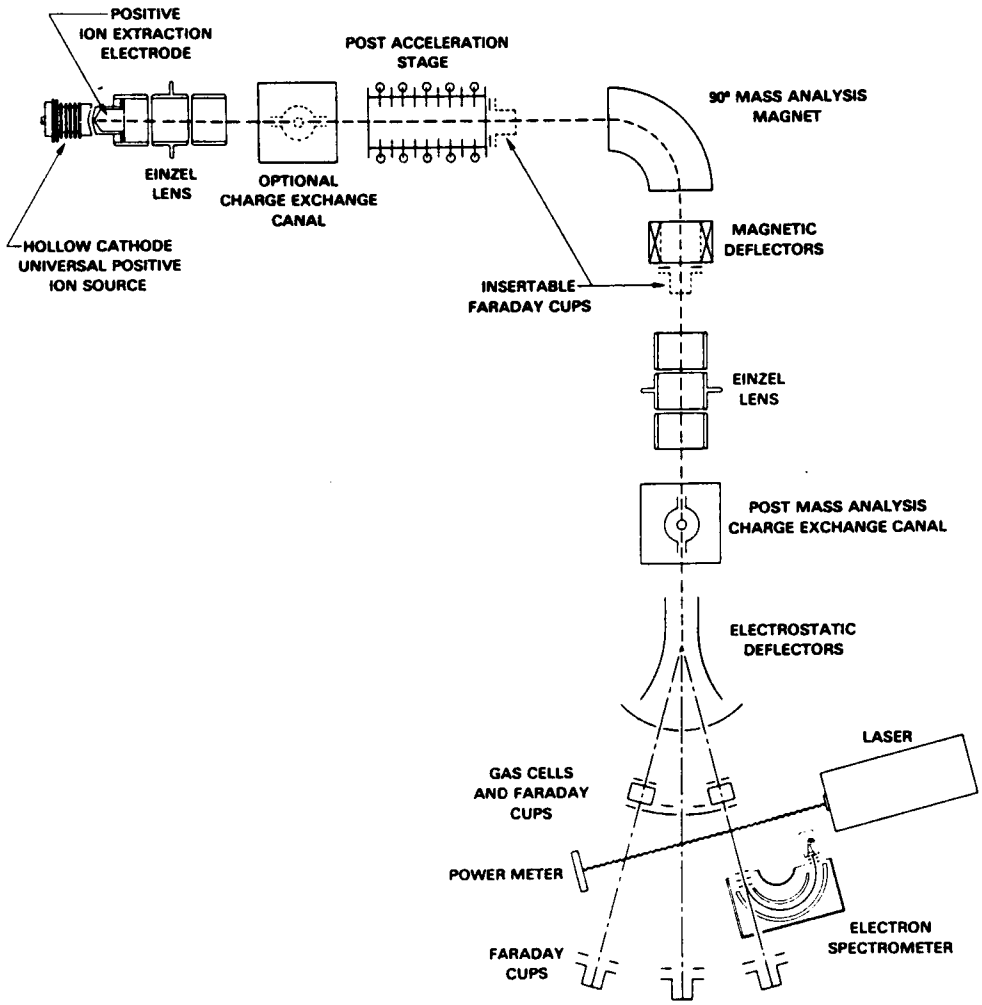


Figure 3.2: Schematic of the ion accelerator

a copper–clad stainless steel oven that operates at temperatures between 300°C and 700°C. Two wick–lined stainless steel tubes connect the oven with a pair of end heaters. The end heaters are operated at a temperature (~325°C) so that the lithium vapor condenses on the end heaters and travels down the wick back into the oven. The two stainless steel tubes and the oven define the region of ion beam–lithium target atom collisions to be a 0.79 cm diameter by 8.25 cm long cylinder.

The sequential double electron capture process used in the present experiments to produce negative ions was first investigated experimentally by Donnally and Thoeming [29] in the formation of He^- using cesium vapor. Investigations by other groups have since been made studying the efficiency and energy dependence of producing He^- by charge exchange using lithium, sodium, and magnesium [30], potassium [31], rubidium [32], and cesium [33] vapors. A study has also been made of the effects of the ion beam energy and charge exchange vapor number density on the production of Ca^- by charge exchange using lithium vapor [24].

In these experiments, it has been found that for an incident He^+ beam at 20 to 40 keV and lithium in the charge exchange cell, the maximum measured production of negative ions (~1.5% of the incident He^+ beam) occurs at an oven temperature of ~585°C. For a Ca^+ beam at 60 to 80 keV, the maximum measured production of negative ions using lithium vapor as the charge exchange medium (~0.4% of the incident Ca^+ beam) occurs at an oven temperature of ~625°C.

After exiting the charge exchange canal, the positive, negative and neutral beams travel approximately one half meter before entering the experimental chamber. As ions in the beams enter the chamber they experience a force produced by the electric field between a pair of electrostatic deflectors. The voltage on the deflectors of this charge–state selector separates the positive, neutral and negative components. The charged beams are deflected ±10° relative to the initial

ion beam direction. The deflectors are enclosed in a grounded aluminum box to minimize the leakage of the electric field into the experimental chamber. The positive and negative ions are collected and monitored by biased and shielded Faraday cups.

After deflection, the negative beam travels approximately one third meter before crossing the photon beam from the laser. The beams interact 2.02 cm in front of the entrance aperture to the electron spectrometer at a measured crossing angle of $89.5 \pm 1.5°$. Photoelectrons emitted in a half angle of $\sim 1°$ with respect to the ion beam direction in the laboratory frame will pass through the 1 mm entrance aperture and into the electron spectrometer. The negative ions and the small fraction of atoms produced by detachment processes pass through the electron spectrometer and into the Faraday cup.

Three sets of mutually perpendicular Helmholtz coils are used to minimize stray magnetic fields inside the experimental chamber. Initial (coarse) current settings on the Helmholtz coils were determined by investigating the magnetic fields in the chamber with a Hall probe, and adjusting the coil currents to reduce the magnetic field to less than 0.05 G in the interaction region. Finer adjustments in the current settings were made while monitoring a photoelectron signal so that the count rate is maximized and the line shape is undistorted. This "fine tuning" is performed periodically and the changes in coil currents have been minor. Care has been taken to ensure that all of the components inside the experimental chamber are non–magnetic.

The accelerator and beam line are separated into three vacuum sections in order to achieve a uniform operating pressure for accelerating and maintaining an ion beam. The sections can be isolated by pneumatically–inserted sliding gate valves and are divided as follows: the accelerator section (including the ion source, extractor, Einzel lens, and acceleration stage), the magnet chamber, and

the downstream beam line (including the Einzel lens, lithium vapor charge exchange cell, and the experimental chamber). All three sections are pumped by oil–filled diffusion pumps which are capable of 2400 ℓ/s pumping speeds. The diffusion pumps are backed by belt–driven rotary vane fore–pumps. The accelerator section has a typical base pressure of $\sim$5 x 10^{-7} Torr, which rises to $\sim$2 x 10^{-5} Torr when a support gas is leaked into the ion source. The magnet section has a base pressure of $\sim$2 x 10^{-8} Torr and the pressure does not rise significantly when the ion source is operating. By using a liquid nitrogen cold trap above the diffusion pump, the pressure in the downstream beam–line can be lowered from the base pressure of $\sim$2 x 10^{-7} Torr to $\sim$2 x 10^{-8} Torr. Photoelectron spectra have been taken with and without the cold trap in use and there is no discernible difference in the measured photoelectron signal or background contribution.

3.3 Laser and Optics

A Candela Corporation LFDL-8 flashlamp–pumped dye laser was used as the source of the photon beam for the photodetachment experiments described in this thesis. Photodetachment cross sections, being associated with a bound–free transition, are inherently low (on the order of 10^{-17}–10^{-18} cm^2) and the negative ion beam currents in these experiments are small (on the order of 0.01 to 0.1 nA). The photon flux must be high to offset these limitations. The laser used in this work also has a pulse duration that is long compared to the transit time of the ions through the laser field so that there is a non–negligible probability of a negative ion being in the photon–ion interaction region when the laser is firing. A dye laser also provides the wavelength tunability necessary to study photodetachment as a function of the incident photon energy.

The dye in the LFDL-8 is excited by a xenon–filled linear flashlamp, firing at a repetition rate of up to 10 Hz with a pulse duration of 2.2 μs. Dye solution

is circulated through the dye cell at a flow rate that is sufficient to replace the excited dye material during the time the flashlamp is off.

The accessible wavelength range of the laser is approximately 350-700 nm, but below ~500 nm the lifetime of dyes against photodegradation is short. A specific wavelength is obtained by selection of the appropriate dye material. The spectral bandpass of the output of the laser was determined by either an intracavity prism tuner or a birefringent filter. In the case of the filter a bandpass of ~0.2 nm was obtained. In the more commonly used configuration, which employed the prism tuner, the bandpass was ~0.5 nm. The laser's peak power varies from typically 400 kW for the red dyes to 100 kW for the blue dyes. For the experiments discussed in this thesis, a peak power of ~150 kW (2–3 W of average power) of laser output has proven sufficient to provide a reasonable photoelectron count rate. The laser beam has a 6 mm diameter and a specified linear polarization ratio of 15:1 as it leaves the laser head.

The wavelength of the laser radiation was measured using a 1/3 meter McPherson monochrometer with an EMI 6256S photomultiplier tube as the detector. A small fraction of the output beam of the laser was directed into the spectrometer for this purpose. The wavelength scale of the spectrometer was calibrated using the 623.8 nm line of a HeNe laser and the 514.5 nm and 488.0 nm lines of an Ar^+ laser. Measurements of the wavelength were made to ±0.05 nm.

Two 90° prisms were used to elevate the beam that exited the laser head and horizontally inject it into the experimental chamber. The laser beam is reflected by 90° relative to its incident direction by total internal reflection from the hypotenuse face of the prisms. Prisms were chosen over mirrors because they more closely approximate achromatic reflectors and were less damage prone. By using prisms to direct the beam, the power loss associated with reflection is held to ~8% and the loss is essentially constant over the laser's wavelength range.

A Glan–Taylor polarizing prism was used to set the linear polarization ratio of the photon beam to ~500:1 (see Fig. 3.3). The polarizing prism consists of two 90° calcite prisms forming a rectangular parallelepiped with an air gap between the hypotenuse faces. Being birefringent, the calcite crystal separates the incident light into ordinary and extraordinary rays, and the polarizing prism is designed so that the rays confront the air gap at an angle that exceeds the critical angle for the ordinary ray. In this way the ordinary ray is completely separated from the laser beam by total internal reflection while the extraordinary ray is transmitted. The exiting laser beam is thus linearly polarized.

After leaving the Glan–Taylor polarizing prism the laser beam passes through a double Fresnel rhomb. This device is used to rotate the linear polarization vector up to 180°. The design of a Fresnel rhomb is based on the fact that for total internal reflection, waves polarized in and perpendicular to the plane of incidence undergo a different phase shift [34]. The double Fresnel rhomb is mounted in a split–ring rotator so that the angle between the polarization vector of the laser light and the plane of incidence can be varied. The output polarization vector can thus be rotated up to 180° relative to the incident polarization vector. This makes possible the study of the angular distribution of photoelectrons relative to the linear polarization vector of the photon beam.

A 10 cm focal length lens was used to focus the laser beam down to a diameter of approximately 1 mm in the interaction region, which is the same diameter as the ion beam. This effectively increased the photon flux in the interaction region and caused the beams to completely overlap.

Reflections and absorptions in the polarization and injection optics limited the transmitted power of the laser beam into the interaction region to ~35% of the output power of the laser. This corresponds to a minimum peak power of ~50 kW and a minimum peak power density of ~1.5 MW/cm^2 in the interaction

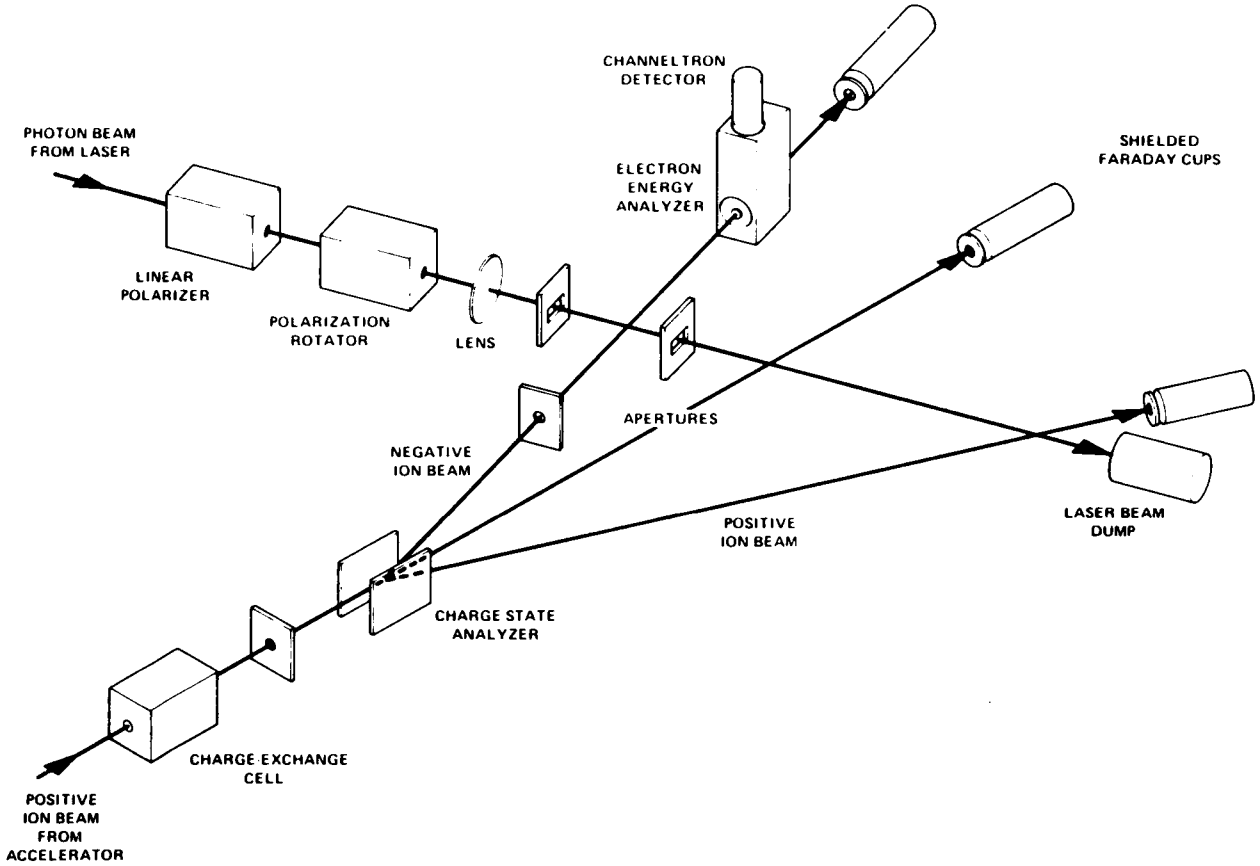


Figure 3.3: Schematic of the crossed–beams apparatus

region. More than half of the loss occurs when the linear polarization of the light is established by the Glan–Taylor polarizer. The remainder of the loss is due to reflection at the air–to–glass interface of the optical components.

3.4 Electron Energy Analyzer

A 160° spherical–sector electron spectrometer was used to analyze the photoelectrons as a function of their kinetic energy. A spherical analyzer provides a radial electric field which linearly disperses charged particles according to their kinetic energy. Aston [35] first suggested using a spherical capacitor as an energy analyzer. Purcell [36] studied the trajectories of charged particles in a spherical capacitor and discussed the physical features of a spherical spectrometer. Since then many authors have used and described the spherical–sector spectrometer for energy analyzing charged particles (see Ref. [37] and references therein), and specifically to energy analyze electrons (see Ref. [38] and references therein).

A spherical–sector analyzer consists of a section of two concentric, conducting spherical surfaces. The gap between the spheres has an inner radius of a and an outer radius of b (see Fig 3.4). For a voltage difference ΔV across the spheres, the potential in the gap can be written as,

$$\phi(r) = -\left[\frac{ab}{a-b}\right]\frac{\Delta V}{r} + C \tag{3.1}$$

where r is the distance from the center of the spheres. The integration constant C is

$$C = \left[\frac{ab}{a-b}\right]\frac{\Delta V}{\bar{r}} \tag{3.2}$$

where $\bar{r} = (a+b)/2$, is the mean radius of the spectrometer. Using Eq. 3.1 the magnitude of the electric field between a and b can be written as

$$E(r) = -\left[\frac{ab}{a-b}\right]\frac{\Delta V}{r^2}. \tag{3.3}$$

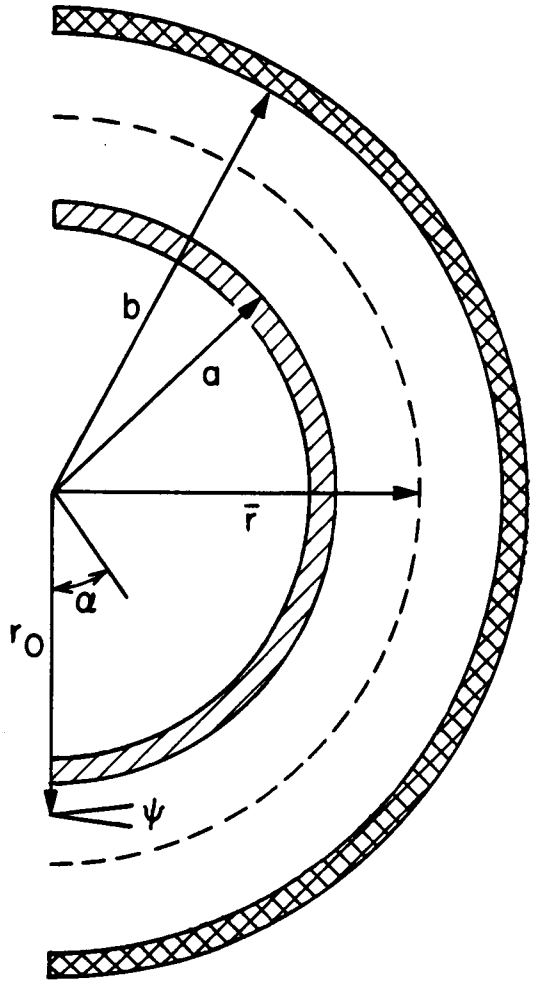


Figure 3.4: Schematic of a spherical–sector analyzer

For an electron to travel through the spectrometer with a trajectory such that it stays on the constant radius $\bar{r}$, the force on the electron from the electric field must equal the centrifugal force associated with this orbit, i.e.

$$e\left[\frac{ab}{b-a}\right]\frac{\Delta V}{\bar{r}^2} = m\frac{v^2}{\bar{r}}, \tag{3.4}$$

where v is the velocity of the electron and m is the electron's mass. The expression can be simplified by using $\bar{r} = (a+b)/2$ and $v^2 = 2(K_0/m)$, where K_0 is the kinetic energy of the electron for the orbit $r = \bar{r}$. This substitution leads to

$$e\left[\frac{ab}{b^2-a^2}\right]\Delta V = K_0. \tag{3.5}$$

The analyzer constant for a spectrometer, B, is defined as

$$B = \frac{e\Delta V}{K_0}. \tag{3.6}$$

For a spherical–sector spectrometer $B = (b/a - a/b)$. For a given spectrometer the analyzer constant defines the relationship between the voltage across the spheres, ΔV, and the necessary kinetic energy (pass energy) for an electron to pass through the spectrometer. The analyzer constant of the spherical–sector spectrometer used in this experiment was measured to be 2.36. This number was obtained by measuring the ΔV required for collisionally detached electrons of known energy from a beam of He^- to pass through the spectrometer. The data was taken with beam energies ranging from 20 to 100 keV.

In order to study the focusing properties of a spherical–sector analyzer, it is necessary to find an equation for r as a function of the angle, α, between the initial and final positions of an electron transmitted through the analyzer. In the case of the central force potential that applies to this problem, it can be shown [39] that the equation of the orbit is

$$\frac{d^2u}{d\alpha^2} + u = -\frac{m}{\ell^2}\frac{d}{du}\Theta\left(\frac{1}{u}\right) \tag{3.7}$$

where $u = 1/r$, Θ is the potential as a function of r, and ℓ is the angular momentum of the orbiting particle. It is instructive to substitute the variable $U = r_0/r$ for u in Eq. 3.7, where r_0 is the radius at which the electron enters the spectrometer. Eq. 3.7 then becomes

$$\frac{d^2U}{d\alpha^2} + U = -\frac{m}{\ell^2}\frac{d}{dU}\Theta\left(\frac{1}{U}\right). \tag{3.8}$$

When an electron enters the spectrometer at a radius r_0 at an angle ψ relative to the mean radius (see Fig. 3.4) the orbit equation (Eq. 3.8) becomes

$$\frac{d^2U}{d\alpha^2} + U = \frac{\overline{r}K_0}{\overline{E}r_0\cos^2\psi} \tag{3.9}$$

where $\overline{E} = E(\overline{r})$. This equation can solved for U,

$$U = \frac{\overline{r}K_0}{\overline{E}r_0\cos^2\psi}(1 - \cos\alpha) + \cos\alpha - \tan\psi\sin\alpha. \tag{3.10}$$

Notice that for $\alpha = 180°$ all of the first order terms in ψ are zero, so the analyzer provides first order focusing in the plane of the analyzer. Due to symmetry, a spherical spectrometer also has first order focusing in the direction perpendicular to the plane of the analyzer.

A 180° spherical–sector energy analyzer, although possessing excellent focusing properties, is difficult to use experimentally. The image and object planes are inside the electric field regions of the spectrometer. Holes would have to be drilled in the spectrometer for the laser to cross the ion beam in the object plane of a 180° analyzer. This would distort the electric field at the object point. For this work, a 160° spherical–sector spectrometer was used. A 160° analyzer removes the object point from inside the analyzer[40] and, at the same time, preserves the focusing properties of a 180° analyzer to a good degree.

A schematic of the spherical–sector energy analyzer, the electron detector, and the voltage power supplies used in the thesis work is shown in Fig. 3.5. The inner radius, a, of the spectrometer is 1.75 cm and the outer radius, b, is 4.76 cm.

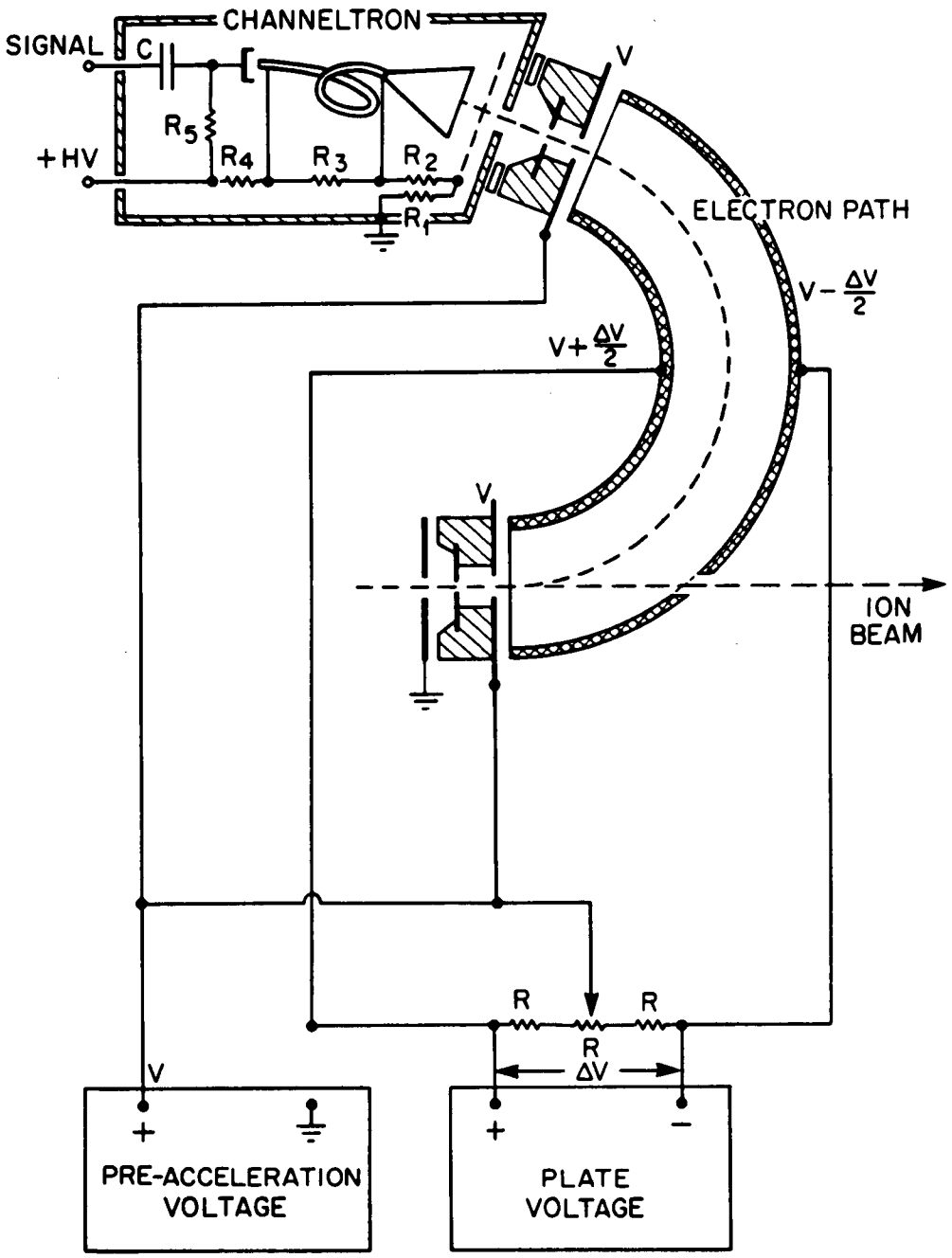


Figure 3.5: Spherical–sector electron spectrometer

The entrance and exit apertures are 1 mm in diameter. The spectrometer is made from OFHC copper and the surfaces are coated with graphite.

The spectrometer was operated in the fixed pass–energy mode [37]. The incoming electrons are accelerated by a voltage V on the entrance apertures so that all incident electrons are analyzed at a constant pass energy. The same voltage is applied to the exit aperture. The spheres are operated symmetrically in voltage about the entrance and exit aperture voltage (i.e. $V \pm \Delta V/2$) so that the potential along the central path is V. The voltage across the spheres, ΔV, was split so that the inner and outer spheres were symmetric in voltage. In this way the electrons enter the spectrometer and travel approximately on an equipotential at the same potential as the entrance aperture.

Spectra are taken by choosing a value of the voltage across the spheres appropriate for the range of kinetic energies of the electrons that are to be studied (see Eq. 3.6). By ramping the acceleration voltage, V, a spectrum of the number of photoelectrons versus their kinetic energy is obtained. It is difficult to measure the kinetic energy of a single peak in a spectrum due to unknown offsets in the energy scale resulting from contact and surface potentials. In the present work only the difference in energy between two close lying peaks have been measured. Under these circumstances the unknown offsets are expected to cancel.

The spherical–sector spectrometer had a measured spectral resolution of $\sim$3%. The measured resolution of a spectral peak depends on the intrinsic resolution of the electron analyzer and contributions associated with dispersion in the photoelectron source parameters such as spreads in ion beam velocities.

After transmission through the spherical–sector analyzer, the photoelectrons were detected by a Galileo Optic Model 4028 channel electron multiplier (CEM). The CEM amplifies the number of incident photoelectrons as a result of the emission of secondary electrons. These electrons are accelerated throughout

the detector by a high voltage placed across the resistive CEM. The gain of the CEM was $\sim 10^8$ in these experiments. Each pulse of electrons that exits the detector is processed in the electronics chain described in the next section and then registered as a photoelectron count.

3.5 Electronics and Data Acquisition System

After the photoelectrons have been energy analyzed by the electron analyzer and detected by the CEM, the detector's output signal must be processed and stored in a manner consistent with the aims of the experiment. For the experiments described in the thesis, the number of photoelectrons detected by the CEM were measured versus the voltage applied to the electron spectrometer. The interest is not only in knowing the voltage where the maximum photoelectron signal occurs, but also in how many photodetachment events occur for a given ion beam density and laser beam flux. This requires monitoring the intensities of both of the crossed beams and discriminating against the contribution to the electron signal that is not associated with photodetachment.

In order to design an efficient scheme for detecting photodetachment events, it was necessary to first make an estimate of the expected photoelectron count rate. The number of photoelectrons that one can expect to detect per laser pulse can be calculated using the following equation [41],

$$S = \Phi \sigma T N_i Q, \tag{3.11}$$

where S is the number of detected photoelectrons per laser pulse, Φ is the photon flux, σ is the total cross section for photodetachment, T is the time that a ion is in the photon beam, N_i is the number of ions that cross the photon beam during the time the laser is on, and Q is an estimated efficiency factor that relates the number of photoelectrons produced to the number that are detected by the CEM.

A sample calculation for the photoelectron count rate for a 30 keV He^- beam demonstrates the importance of the design of the electronics used to record photodetachment signals. The photon flux (Φ) is the number of photons per square meter per second and can be written as

$$\Phi = \frac{W}{AE_\gamma}, \tag{3.12}$$

where W is the peak power of the laser in watts, A is the cross sectional area of the laser beam in square meters, and E_γ is the photon energy in joules. The peak power of the laser for these experiments is ~50 kW at the interaction region where the laser beam is focused down to a spot size of 10^{-3} m in diameter. For a photon energy of 3.37 x 10^{-19} J (590.0 nm), the photon flux at the photon–negative ion interaction region is 2 x 10^{29} photons/m^2-s. The cross section, σ, for photodetachment of He^- is of the order 10^{-21} m^2 (10^{-17} cm^2) [42]. In a crossed beams experiment using a pulsed laser, the interaction time (T) is the shorter of either the pulse length of the laser or the transit time for an ion to cross the laser beam. A 30 keV He^- ion takes 8.33 x 10^{-10} s to travel the 10^{-3} m diameter laser beam, which is a much shorter time than the 2.2 x 10^{-6} s pulse duration of the laser. Multiplying the photon flux by the cross section and interaction time gives the probability for photodetachment per beam ion (P) and can be written as

$$P = \Phi\sigma T. \tag{3.13}$$

For this sample calculation $P \sim 0.1$. The number of ions that cross the photon beam during the laser pulse, N_i, can be written as

$$N_i = \frac{I\tau}{(e)} \tag{3.14}$$

where I is the ion beam current in amperes, τ is the laser pulse duration in seconds, and e is the unit of charge in coulombs. For a ~10^{-10}A beam and a laser

pulse duration of 2.2 x 10^{-6} s, $N_i \sim 10^3$ ions. The efficiency factor, Q, is the product of the solid angle for collection of electrons by the electron spectrometer, the transmission of electrons through the electron spectrometer and the detection efficiency of the CEM. Q is estimated to be on the order of 10^{-3} based on knowledge of the solid angle of collection. Substituting into Eq. 3.11 the values of Φ, σ, T, N_i and Q leads to a value of S, the number of detected photoelectrons per laser pulse, of $\sim$0.1.

Using this value of S and integrating over 200 laser pulses leads to a maximum photoelectron signal of 20 counts per channel. The geometry of the experiment (the negative ion beam travels through the electron spectrometer) leads to a background electron count rate, associated with the ion beam striking apertures and collisional detachment, of approximately 1 kHz. With the laser operating at 10 Hz it takes 20 seconds to collect 20 photoelectron counts. During this time the number of background electrons collected is 2 x 10^4. Thus the signal–to–noise ratio is $\sim 10^{-3}$. The situation can be vastly improved if a detection scheme is used that discriminates between photoelectrons and electrons created by other processes.

The electronics system was designed to take advantage of the fact that the photoelectron signal is synchronous with the time structure of the pulsed laser and that the source of the background, the ion beam, is continuous. A schematic of the electronics system of this synchronous detection scheme is shown in Fig. 3.6. The electronics consist of four input channels and one output channel connected to a CAMAC–based multichannel analyzing data acquisition computer. The data is collected by four LeCroy 3521A multichannel scalars (MCS).

The output of the CEM detector was amplified by an ORTEC 113 preamplifier and an ORTEC 410 linear amplifier. The dual purpose of the ORTEC 436 discriminator was to eliminate most of the low amplitude noise generated in the

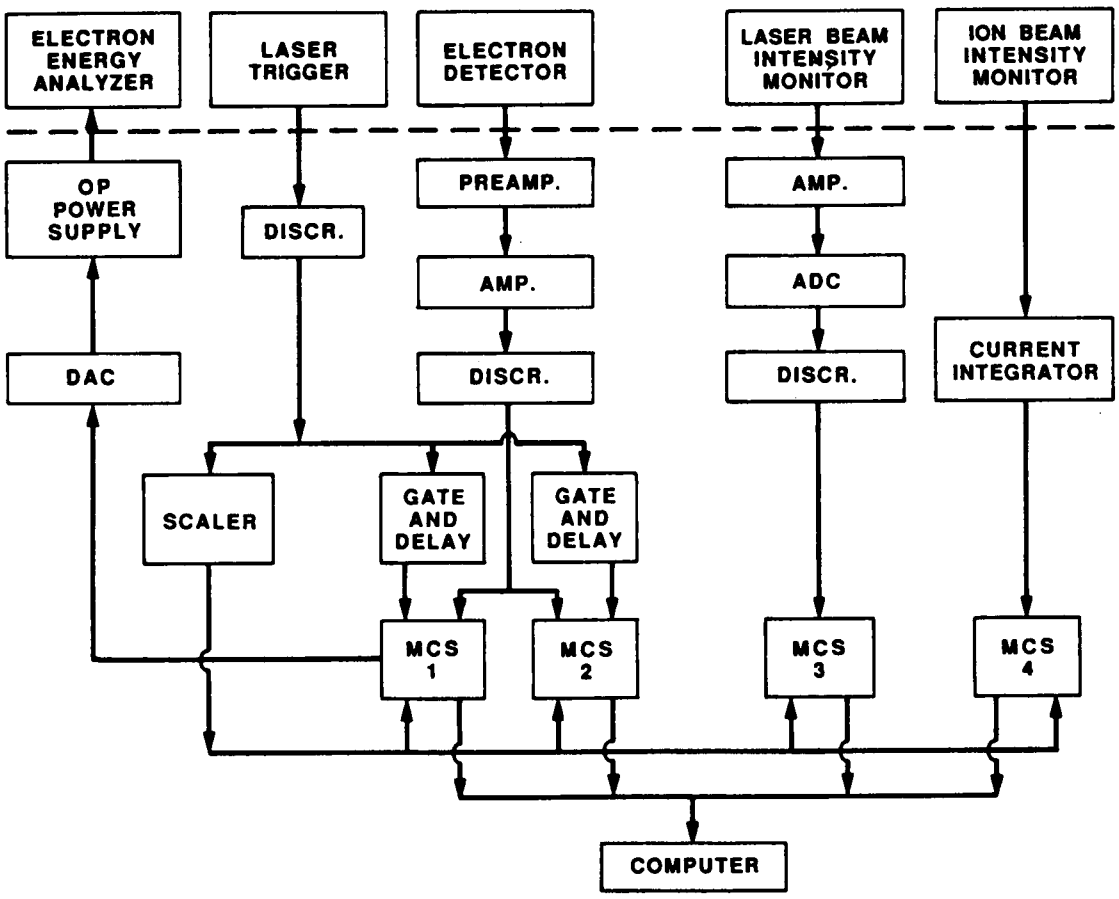


Figure 3.6: Electronics and data acquisition system

amplification stages and create an output pulse that was compatible with the input requirements of an MCS. The electron signal was collected by both MCS1 and MCS2.

An EG&G FND–100 fast photodiode was used to obtain a master trigger pulse for the synchronous detection of photoelectrons. The photodiode gave an output voltage pulse each time the laser fired. This pulse was used to start two ORTEC 416 gate–and–delay generators that, in turn, activated MCS1 and MCS2. A timing diagram is shown in Fig. 3.7. The t=0 reference point is set by the firing of the laser trigger photodiode. One gate–and–delay generator opened MCS1 for a duration of 4 μs after a delay of 3.2 μs. This delay was set to allow for the finite transit time of the photoelectrons from the interaction region to the detector. MCS1 collected the electron signal associated with the laser firing and the background signal in this 4 μs gate. The second gate–and–delay generator opened MCS2 for a duration of 4μs after a delay of 9.2μs. MCS2 collected, in the absence of the laser pulse, the background signal that occurs in 4μs. Because the background was associated with a continuous source, the background signals collected by MCS1 and MCS2 were equal. By subtracting the contents of the two multichannel scalars, the background contribution was eliminated, leaving only the photoelectron signal. This method of synchronous detection led to a signal–to–noise ratio of $\sim 10^2$, five orders of magnitude greater than that mentioned previously in Section 3.5.

The integration time per channel of the MCS's was controlled by an ORTEC 776 scalar. The output pulses from the FND–100 photodiode were monitored and counted by the scalar. These pulses were used to set the dwell time per channel of the four MCS's. After a preset number of laser firings, the scalar cleared itself and sent an output pulse to advance the channel of the multichannel scalars. When MCS1 received this signal, it emitted a digital signal which,

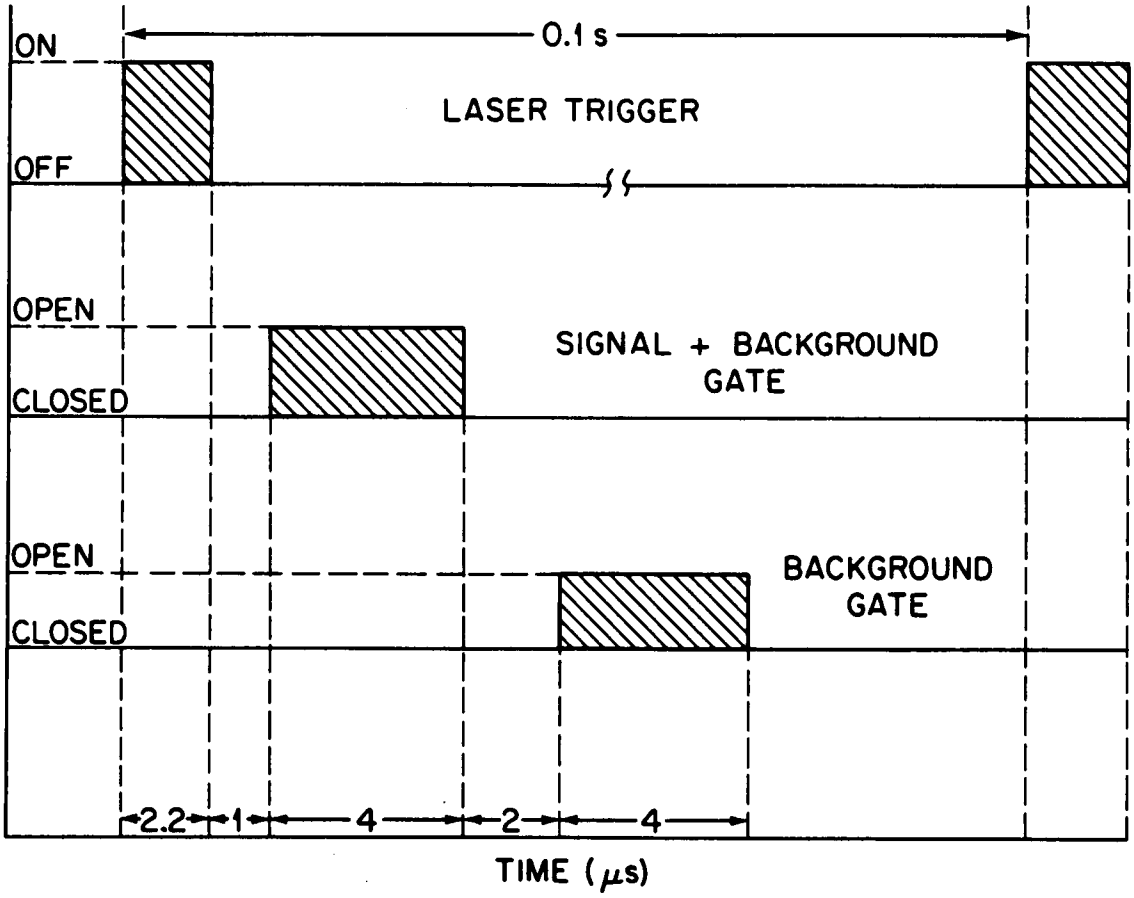


Figure 3.7: Timing diagram for the synchronous detection of photoelectrons

after conversion by a digital–to–analog converter (DAC), advanced the voltage on the electron spectrometer. The resolution of the DAC limited the finest voltage steps in these experiments to 0.024 V. The process of simultaneously advancing the multichannel scalars and the voltage on the spectrometer occurred after the gate to MCS2 closed and before the next pulse from photodiode arrived.

The negative ion beam intensity was monitored using the Faraday cup behind the electron spectrometer (see Fig. 3.2). The cup was shielded and contained a negatively biased guard ring to prevent secondary electrons from escaping. The output signal from this Faraday cup was routed to an ORTEC 439 Digital Current Integrator. The ORTEC 439 put out a logic pulse after collecting a preset amount of charge. These pulses were collected and recorded by MCS3. For each channel in MCS1, the ion beam intensity was recorded in a corresponding channel in MCS3. This made it possible to correct for fluctuations in the ion beam intensity.

The laser beam intensity was monitored by an EG&G UV–100 photodiode. The photodiode emitted a voltage pulse when the laser fired that was proportional to the laser beam intensity. The voltage pulse was converted to a train of logic pulses by an analog–to–digital converter (ADC). The number of logic pulses was proportional to the pulse height (voltage) of the output from the photodiode. The number of logic pulses produced by the ADC was recorded by MCS4. Care was taken to ensure that the voltage of the output pulse from the photodiode varied linearly with the measured laser beam intensity over the range of laser powers used in these experiments. The contents of MCS4 were used to normalize the number of photoelectron counts recorded by MCS1 to the fluctuations in the laser beam intensity.

The four multichannel scalars were connected to a LeCroy 3500 multichannel analyzing computer via a CAMAC dataway. The computer was used to store and view the data.

CHAPTER 4

ELECTRON AFFINITY OF THE CALCIUM ATOM

4.1 Introduction

The formation of a stable negative ion of a Group IIA element would involve the attachment of an electron to the (ns^2) ^1S ground state of the parent atom. As a result of the Pauli exclusion principle, the extra electron is forced to enter a subshell different than that occupied by the atomic valence electrons. Calculations have supported the general belief that, under such circumstances, the enhanced screening of the nuclear charge by the atomic electrons would be effective in prohibiting stable negative ion formation [4], [43].

Be^- and Mg^- are known, for example, not to have bound ground states. The $(2s^22p)$ ^2P state in Be^- has been shown to lie $\sim$ 0.5 eV above the ground state of Be [44], [45]. Similarly, the $(3s^23p)$ ^2P state in Mg^- has been detected as a shape resonance in the electron–atom elastic–scattering cross section at $\sim$0.15 eV [46].

In the case of Ca^-, the most obvious candidate for the ground state of the ion would be the $(3d4s^2)$ ^2D state since this is the ground state of the isoelectronic Sc atom. This state, however, appears not to be bound in the case of Ca^-. Due to the short–ranged nature of the binding force in negative ions, core penetration effects become very important. The 3d orbital is not as effective at penetrating the screening of nuclear charge as the 4p orbital. However, Kurtz and Jordan [47] did not predict the $(4s^24p)$ ^2P state to be bound. It appears that these and earlier calculations failed to take into account all of the correlation inherent in this system.

The existence of long lived alkaline earth negative ions has been known experimentally for some time. Heinicke et al. [48] extracted negatively charged Group IIA elements from a cold–cathode Penning–discharge ion source. The life-

times of these ions were estimated to be at least on the order of microseconds based on time of flight arguments. In an attempt to explain the experimental observations, Weiss [49] performed calculations on metastable states of Be^- and Mg^-. The study found that the lowest bound excited states of Be^- and Mg^- were the $(2s2p^2)\ ^4P$ and $(3s3p^2)\ ^4P$ states, respectively. Subsequently, Bunge [50] predicted that the Ca^- ion could be formed in the $(4s4p^2)\ ^4P$ state. These ^4P excited states are metastable because autodetachment to the atomic ground state is spin forbidden.

Using the technique of autodetachment spectroscopy, Kvale et al. [25] showed that Be^- exists in the metastable $(2s2p^2)\ ^4P$ state. An attempt to detect the autodetached electron signature associated with the decay of the $(4s4p^2)\ ^4P$ state in Ca^-, however, was unsuccessful [51]. Calculations have shown that the lifetimes of the levels of the Be^- metastable state are between 10^{-3} and 10^{-8} s [52]. The lifetimes of the levels of the Mg^- metastable state have been calculated to be in the range of a nanosecond [53]. Subsequently, it has been shown by Beck [54] that the lifetimes of the levels associated with the metastable state in Ca^- were reduced to the sub–nanosecond range by the enhanced strength of the magnetic interactions that drive the autodetachment process. In the apparatus used to search for the autodetaching electrons from Ca^-, the time delay between the production of the ions and their detection was a few microseconds. It thus became clear that metastable states such as the $(4s4p^2)\ ^4P$ state could not be responsible for the long–lived Ca^- ions observed in previous studies [24], [48], [55].

This chapter shows, contrary to earlier predictions, experimental evidence for a stable Ca^- ion. The structure of Ca^- has been experimentally determined by Pegg et al. [56], who find the ion to be stably bound in the $(4s^24p)\ ^2P$ state. This result was concurrently confirmed theoretically by Froese Fischer et al. [57] and later by Krylstedt et al. [58].

4.2 Photoelectron Spectroscopy

The photoelectron spectroscopy measurements described in this chapter were made using the crossed–beams apparatus described in Chapter 3. A beam of Ca^- ions was produced by passing a beam of Ca^+ ions with a kinetic energy of 60 to 80 keV through a lithium vapor cell. The conversion efficiency was found to be on the order of 1%. The Ca^- ion beam current at the interaction site was typically 0.01 nA. Just prior to the entrance of the electron spectrometer, the ion beam was crossed perpendicularly with the photon beam from a flashlamp–pumped dye laser.

Photoelectrons ejected in the field–free interaction region in the direction of the ion beam entered the electron spectrometer and were detected. The electron spectrometer was operated in a fixed pass–energy mode. A spectrum of the photoelectron signal versus the laboratory kinetic energy of the electrons was obtained by ramping the voltage on the entrance aperture of the spectrometer. The voltage was incremented in steps of either ~0.024 V or ~0.048 V. The background electron signal, which was continuously distributed in energy and time, was associated with electrons generated by ion impact with apertures and collisional detachment with residual gas. It was subtracted from the photoelectron signal. The ion beam intensity was recorded so that the photodetachment signal could be normalized to fluctuations in the ion beam intensity.

The photoelectron kinetic energy, E_c, as measured in the rest frame of the ion, is related to the electron affinity of the residual atom, E_a, by

$$E_a = E_\gamma - E_e - E_c \tag{4.1}$$

where E_e is the excitation energy of the residual atom relative to the atomic ground state, and E_γ is the photon energy. In the laboratory reference frame, the kinetic energy, E_l, of electrons photodetached from an ion of kinetic energy, E_i, is

related to the electron energy in the rest frame of the ion, E_c, by the kinematic transformation equation (see Section A.2)

$$E_l = E_c + \epsilon \pm 2\sqrt{\epsilon E_c}\cos\theta_c. \tag{4.2}$$

In this equation θ_c is the angle of ejection of the photoelectrons in the ion frame. The quantity, $\epsilon = (m_e/M_i)E_i$, is the laboratory energy of electrons traveling at the same velocity as the ions in the beam, i.e. E_c=0. Under the conditions of the present experiment, i.e. $\theta_l = 0$, Eq. 4.2 reduces to the form

$$E_l = E_c + \epsilon \pm 2\sqrt{\epsilon E_c}. \tag{4.3}$$

Fig. 4.1 shows an electron energy spectrum obtained by crossing a 60 keV Ca^- ion beam with laser light of wavelength $\lambda = 635.2 \pm 0.2$ nm. The three peaks 1, 2, and 3 occur at 0.62 eV, 1.06 eV, and 5.24 eV, respectively, in the laboratory frame. In the ion reference frame the difference in energy between peaks 2 and 3 is found to be equal to the excitation energy of the (4s4p) ^{3}P state of Ca above the ($4s^2$) ^{1}S ground state. The separation of peaks 2 and 3 therefore permits one to unambiguously identify the two photodetachment channels that are accessible at this photon energy. Peak 3 corresponds to the process in which the residual Ca atom is left in the ground state, i.e. $Ca^- + h\nu \longrightarrow Ca(4s^2)\ ^1S + e^-$. Peaks 1 and 2 are both associated with the photodetachment channel $Ca^- + h\nu \longrightarrow Ca(4s4p)\ ^3P + e^-$. The strength of peak 2 eliminates one of the two possible configurations for the stable state of Ca^-. The strong signature associated with this photodetachment channel that leaves the atom in the (4s4p) ^{3}P state indicates that Ca^- must be formed in the ($4s^24p$) ^{2}P state. The selection rules for photodetachment [59] forbid a transition from the ($3d4s^2$) ^{2}D ion state to the (4s4p) ^{3}P atomic state.

The reduced ion beam energy, ϵ, is ~0.82 eV for a 60 keV Ca^- beam. Thus the laboratory kinetic energy that corresponds to an ion frame kinetic energy

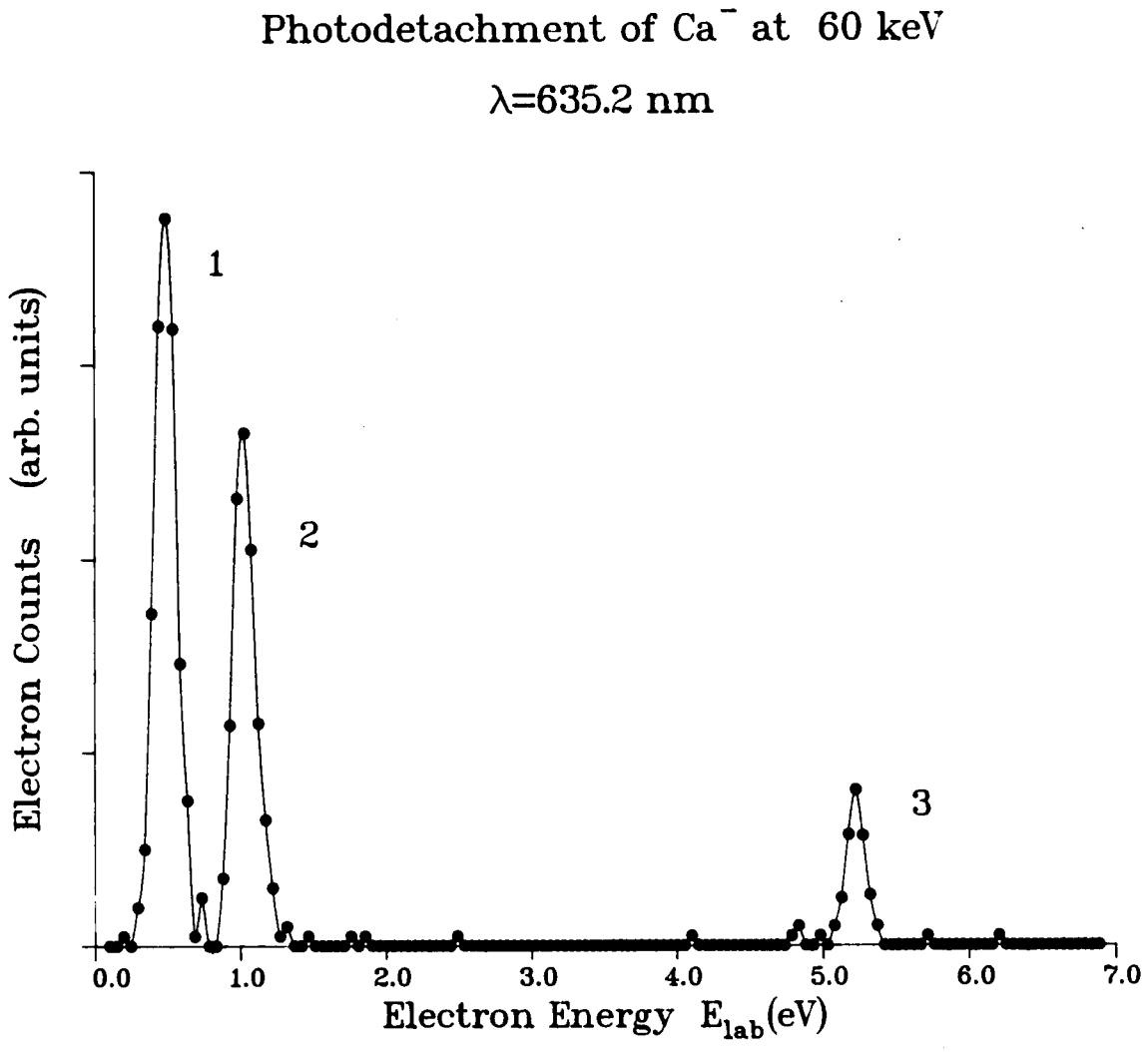


Figure 4.1: A typical kinetic energy spectrum of photoelectrons produced in the process, $Ca^- + h\nu \longrightarrow Ca + e^-$. Peaks 1 and 2 are associated with the photodetachment channel leaving the Ca atom in the ^3P state. Peak 3 corresponds to the photodetachment channel leaving the Ca atom in the ^1S state.

equal to zero lies between peaks 1 and 2. At this photon energy the ion frame kinetic energy, E_c, of an electron photodetached in the process $Ca^-(4s^24p)\ ^2P + h\nu \longrightarrow Ca(4s4p)\ ^3P + e^-$ is approximately 15 meV. In this case the condition $v_i > v_c$ is met, making peak 1 the kinematically doubled partner of peak 2 (see Section A.2). The backward–directed electrons (peak 1) are "swept" into the electron analyzer by the velocity of the ion beam. Peak 3 does not have a kinematically doubled partner in this spectrum because the ion frame velocity of the photoelectron from the process $Ca^-(4s^24p)\ ^2P + h\nu \longrightarrow Ca(4s^2)\ ^1S + e^-$ is not less than the ion beam velocity (i.e. $v_i < v_c$).Therefore, the backward–directed electrons from this process will not enter the electron spectrometer. It is interesting to note that kinematic effects have "magnified" the ion frame kinetic energy of the slow photoelectrons ($E_c \approx 15$ meV) by a factor of about seventy. This makes the electrons much easier to study experimentally.

4.3 Experimental Results

4.3.1 Data Analysis

The electron affinity of the Ca atom was determined by an analysis of the separations of the forward– and backward–directed photoelectron peaks in many different spectra. Eq. 4.4 and an equation that relates the separation of the two peaks in the laboratory frame to the ion frame kinetic energy of the photoelectrons (see Eq. A.9)

$$E_c = \frac{(\Delta E_l)^2}{16\epsilon} \tag{4.4}$$

were employed to analyze the experimental data. The quantity, ϵ, was determined by directly measuring the ion beam energy. By measuring the difference in energies of two closely lying peaks, one can greatly minimize errors associated with contact and surface potentials in the electron analyzer and eliminate the need for a precise

knowledge of the analyzer constant. The value of E_c was determined by taking photoelectron energy spectra at beam energies of 60, 70, and 80 keV, and photon wavelengths of 595.7 and 635.2 nm.

In order to determine the electron affinity of Ca using Eq. 4.4 the excitation energy, E_e, must be known. Application of the selection rules for the photodetachment process, $Ca^-(^2P_J) + h\nu \longrightarrow Ca(^3P_{J'}) + e^-$, shows that only the J=1/2 to J'=0,1 and J=3/2 to J'=1,2 transitions are allowed. The formalism developed by Engelking and Lineberger [60] was used to calculate the branching ratios for these four transitions and they are listed in Table 4.1. The relative intensities of the fine–structure lines were then calculated on the assumption that the J=1/2,3/2 levels of the $(4s^24p)\ ^2P$ state of Ca^- are statistically populated in the production process. The assumption seems justified since the fine–structure splitting in this case is expected to be small. The relative spacings of the lines should be primarily determined by the fine–structure splittings between the J'=0,1,2 levels of the (4s4p) ^3P state of Ca which are expected to be much larger than the splitting between the J=1/2,3/2 levels of the $(4s^24p)\ ^2P$ state of Ca^-. The electron energy resolution was insufficient to separate the fine–structure components of the peaks. The symmetry of the peaks indicate that the fine–structure lines are completely unresolved and, at least, approximately statistically populated.

The results of these calculations were also used to estimate the relative populations of the J'=0,1,2 levels of the (4s4p) ^3P state of Ca after the photodetachment process. The center of gravity of the fine–structure levels of this state was calculated using the relative populations of the levels and their known spacings [61]. The excitation energy of the J'=1 level of the (4s4p) ^3P state is known from optical spectroscopy to be 1.886 eV [61]. The excitation energy of the center of gravity, appearing in Eq. 4.1, was then determined to be $E_e = 1.894$ eV.

Using this value of E_e, the measured value of E_γ, and a value for E_c

Table 4.1: Calculated branching ratios for the photodetachment of $Ca^-(^2P_{3/2,1/2})$ into the various fine–structure levels of $Ca(^3P_{0,1,2})$

	Branching ratios
$^2P_{1/2}+h\nu \longrightarrow {}^3P_0+e^-$	0.33
$^2P_{1/2}+h\nu \longrightarrow {}^3P_1+e^-$	0.66
$^2P_{3/2}+h\nu \longrightarrow {}^3P_1+e^-$	0.33
$^2P_{3/2}+h\nu \longrightarrow {}^3P_2+e^-$	1.67

determined by Eq. 4.4, one can determine the electron affinity of Ca. The final result was measured to be $E_a(Ca) = 0.043$ eV. This value represents an average of all the data sets, each weighted by the measured uncertainty in E_c. The statistical fluctuations in the data points, the finiteness of the step size and the calibration of the electron energy scale all introduce errors in determining the energy difference between the forward– and backward–directed peaks. These errors produce a small range in the measured value of E_c.

Other methods of analysis of the spectral data were used to cross check the result obtained by the method described above. One method involved measuring the energy separation of the two forward–directed peaks (peaks 2 and 3) corresponding to photodetaching Ca^- into the $(4s^2)\ ^1S$ and $(4s4p)\ ^3P$ states of Ca. Another method of analysis involved the determination of the position of peak 3 (the peak associated with leaving the residual atom in its ground state) relative to a photoelectron peak produced by photodetaching a beam of B^-, whose electron affinity is well known [62]. Both of these alternative methods of analysis, although somewhat less accurate, produced values of the electron affinity of Ca in good agreement with that determined by the measurement using the separation of the forward– and backward–directed kinematically doubled pair of peaks and the ion beam energy.

4.3.2 Error Analysis

An estimate of the uncertainty in the value of the electron affinity of Ca can be found by evaluating the uncertainties associated with the different parameters used to make the measurement. Applying standard propagation–of–error analysis [63] to Eq. 4.1 yields

$$\frac{\delta(E_a)}{E_a} \simeq \frac{\delta(E_\gamma)}{E_\gamma} + \frac{\delta(E_e)}{E_e} + \frac{\delta(E_c)}{E_c}. \tag{4.5}$$

The photon wavelength can conservatively be determined, using a photon spectrometer, to ± 0.2 nm. The error associated with measuring the photon energy is thus

$$\frac{\delta(E_\gamma)}{E_\gamma} = 0.0003. \tag{4.6}$$

Spectroscopic measurements of the excitation energy of the (4s4p) $^3P_1$ state of Ca and the fine–structure splittings between the J'=0 and J'=1,2 levels are quite accurately known [61]. Errors in these quantities are negligibly small compared with the uncertainties in other parameters used in the present measurement. The assumption that the initial state fine–structure levels are statistically populated can be incorporated in the error analysis. An initial state population that is entirely either in the J=1/2 or J=3/2 level of Ca^- can be interpreted as a range error in E_e. These two possibilities correspond to an uncertainty in E_e equivalent to an error of 0.005 eV in the excitation energy. This uncertainty is analogous to an error in determining the excitation energy of

$$\frac{\delta(E_e)}{E_e} = 0.003. \tag{4.7}$$

The uncertainty in measuring the kinetic energy of the photodetached electron depends, according to Eq. 4.4, on the laboratory separation of the forward– and backward–directed peaks, ΔE_l, and the electron equivalent energy of the ion,

ϵ, i.e.,

$$\frac{\delta(E_c)}{E_c} = 2\frac{\delta(\Delta E_l)}{\Delta E_l} + \frac{\delta(\epsilon)}{\epsilon}. \tag{4.8}$$

The estimated uncertainty in determining the ion beam energy from a measurement of the acceleration voltage is approximately 1 keV. The maximum error associated with the determination of ϵ is therefore

$$\frac{\delta(\epsilon)}{\epsilon} = 0.017. \tag{4.9}$$

The error in the measurement of the separation of the photoelectron peaks, ΔE_l, is the uncertainty in determining the centers of the peaks in the electron energy spectrum. The finite resolution of the spectrometer, the statistical fluctuations of the data points, and the voltage step size used in the electron energy scale all contribute to the uncertainties in determining the peak centers. The error in ΔE_l then depends on the uncertainty in determining the peak centers and the separation of the two peaks. A representative value of the error in ΔE_l, for a typical data set, is

$$\frac{\delta(\Delta E_l)}{\Delta E_l} = 0.07. \tag{4.10}$$

This is clearly the major source of uncertainty in the determination of the electron affinity.

Substituting the values of the error in each parameter into Eq. 4.5 yields a fractional error in the measured electron affinity of

$$\frac{\delta(E_a)}{E_a} = 0.16. \tag{4.11}$$

The final measured value of the electron affinity of Ca, which reflects the error in the contributing measurements, is $E_a(Ca) = 0.043 \pm 0.007$ eV.

4.4 Conclusion

Using photoelectron spectroscopy, Ca^- has been shown to be a stable negative ion. This is the first evidence for a stable negative ion of a Group IIA element. The spacing of peaks 2 and 3 in the Ca^- spectrum shows unambiguously that Ca^- is formed in the $(4s^24p)\ ^2P$ state. Fig. 4.2 is an energy level diagram for the lowest lying states of Ca and Ca^-. Electron peaks associated with the two photodetachment channels that are accessible at the photon energies used in these experiments, $Ca^-(4s^24p)\ ^2P + h\nu \longrightarrow Ca(4s^2)\ ^1S + e^-$ and $Ca^-(4s^24p)\ ^2P + h\nu \longrightarrow Ca(4s4p)\ ^3P + e^-$, appear in the electron energy spectrum. The $(4s4p^2)\ ^4P$ metastable state predicted by Bunge [22] has not been ruled out by this experiment. Evidence for the photodetachment of this metastable state was not found in the present experiment. If the metastable state is bound, it must have a lifetime much shorter than a few microseconds, the time delay between its production and the laser–ion interaction region of the present apparatus. Beck [54] has estimated that in Ca^-, the lifetimes of the levels of this metastable state should be reduced to the sub–nanosecond range by the enhanced strength of the magnetic interactions.

The measured electron affinity of Ca is 0.043 ± 0.007 eV. This is the smallest binding energy, that has been measured to date, for a ground state atomic negative ion. The kinematic effects associated with a fast–moving ion beam were exploited to determine the electron affinity of Ca. Kinematics "magnified" the photoelectron kinetic energies and made it possible to use the phenomenon of kinematic peak doubling to determine the electron affinity.

The binding energy of the most loosely–bound electron of a negative ion is difficult to accurately calculate because it is the small energy difference between the large total energies of the ground states of the ion and atom. A Hartree–Fock (central field) calculation finds that the $(4s^24p)\ ^2P$ state of Ca^- lies 0.256 eV above

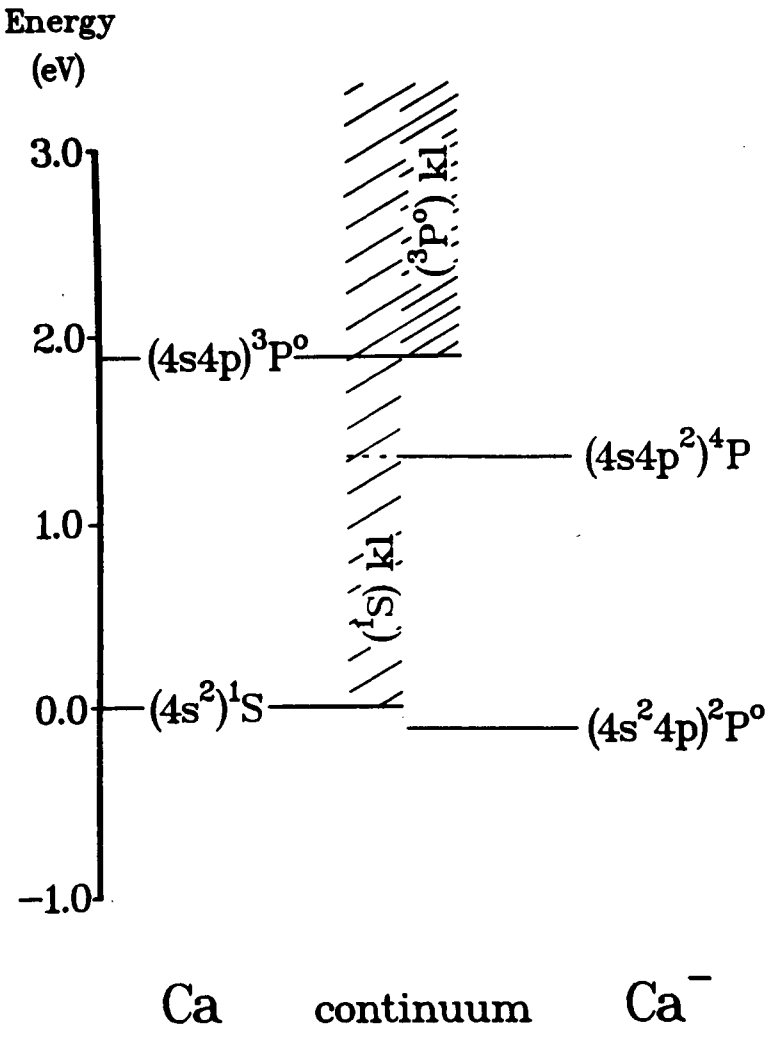


Figure 4.2: Energy level diagram of the lowest lying states of Ca and Ca^-

the ground state of Ca [64]. This is approximately 0.3 eV above the experimentally measured energy level of the $(4s^24p)\ ^2P$ state [56]. Correlation, which takes into account the relative motion and spins of the electrons, must be included for the calculations to be accurate (refer to Section 2.3).

Configuration interaction methods are often used to account for correlation in calculations on multi–electron systems. Froese Fischer et al. [57] have used the multiconfiguration Hartree–Fock (MCHF) method, with a small relativistic shift correction, to calculate the electron affinity of Ca. They predict that Ca^- is formed in the $(4s^24p)\ ^2P$ state and the electron affinity of Ca is 0.045 eV. Froese Fischer [65] has more recently reported a revised value of $E_a(Ca) = 0.062$ eV. These calculations have shown that the dominant configuration in the multiconfigurational wavefunction representing the ion state was the $4s^24p$ configuration. The presence of the nearby configurations containing 3d electrons, however, significantly affected the correlation energy of the ground state of Ca^-. Configurations containing a 3d electron had no effect on the correlation energy of the ground state of Ca. This differential effect is apparently the source of stability in the case of the Ca^- ion. It is expected that a similar stabilizing effect will be present in the negative ions of the Group IIA elements heavier than Ca. In the case of the lighter elements, Be and Mg, configurations containing 3d electrons are highly displaced in energy from the ground state configurations and have little effect on their energies.

Krylstedt et al. [58] used an exterior complex dilated electron–atom scattering model to study the $(4s^24p)\ ^2P$ state in Ca^-. This method is very effective in predicting resonances in electron–atom scattering, a process which is essentially the inverse of photodetachment. Their value for the electron affinity of Ca is 0.055 eV.

The experimentally determined value of the electron affinity of Ca re-

ported in this thesis ($E_a = 0.043 \pm 0.007$ eV) is in good agreement with these calculations. Estimates of the uncertainties in the calculations were not reported for either theoretical investigation.

CHAPTER 5

PHOTODETACHMENT OF He^-: ANGULAR DISTRIBUTION OF PHOTOELECTRONS

5.1 Introduction

In the photodetachment process, energy and angular momentum in the form of a photon are transferred to an electron which is subsequently ejected. The energy and angular momentum of the photoelectrons are manifested in their angular distribution. Thus, the emission pattern of the photoelectrons contains information on the initial and final states as well as information on the dynamics of the emission process.

The differential cross section for ejecting an electron from a negative ion that absorbs a linearly polarized photon is (see Eq. 2.29)

$$\frac{d\sigma}{d\Omega} = \frac{\sigma}{4\pi} f(\theta). \tag{5.1}$$

The function f(θ) describes the angular correlation between the incident photon and the outgoing electron. The angle θ is the angle between the emission direction of the photoelectron and the polarization vector of the incident light. The angular correlation factor can be written in the electric dipole approximation as

$$f(\theta) = 1 + \beta P_2(\cos\theta). \tag{5.2}$$

Here it is assumed that the negative ion is unpolarized (i.e. the magnetic sublevels are equally populated) prior to photoabsorption. In the equation β is an asymmetry (anisotropy) parameter and $P_2(\cos\theta)$ is the second–order Legendre polynomial. The asymmetry parameter completely characterizes the shape of the angular distribution of the photoelectrons.

Angular distributions of electrons photodetached from negative ions were first studied in 1968 by Hall and Siegel [66]. The asymmetry parameters, β, for electrons photodetached from H^- and O^- were determined at a fixed photon energy of 2.540 eV. These investigators also determined the asymmetry parameter for electrons photodetached from C^- at photon energies of 2.540 and 2.406 eV. Calculations, based on an independent electron model by Cooper and Zare [67], were in reasonably good agreement with Hall and Siegel's experimental values. Kasdan and Lineberger [68] later measured angular distributions of electrons photoejected from alkali–metal negative ions using a 2.540 eV photon beam. Moores and Norcross [69] calculated a value of the asymmetry parameter for the process $K^-(^1S) + h\nu \longrightarrow K(^2P) + e^-(ks,d)$ that is consistent with Kasdan and Lineberger's measurement. Angular distribution measurements in the analogous photoionization process have been reviewed by Berkowitz [38].

This chapter describes the spectral dependence of the photoelectron asymmetry parameters for the two photodetachment channels of the metastable He^- ion that are open in the range of photon energies used in this experiment. With the exception of H^-, He^- represents the simplest system for probing the effects of correlation on electron emission following photodetachment. He^-, even though it is metastable, has been one of the most studied negative ions.

The He^- ion was first experimentally detected in mass spectrometry measurements by Hiby [70]. Subsequently Holøien and Mitdal [71] performed a calculation that showed the core–excited (1s2s2p) ^4P state of He^- should be metastable. The (1s2s2p) ^4P state is formed when an electron attaches itself to the (1s2s) ^3S metastable excited state of He. Consequently, the ^4P state is unstable against autodetachment. This spin–aligned quartet state is metastable, however, since it is embedded in a doublet continuum. As a result, the allowed autodetachment process induced by the strong electrostatic interactions among the electrons is

forbidden. Thus the ^4P state decays via a forbidden autodetachment process induced by the weaker magnetic interactions. Physically, the autodetachment of this spin–aligned quartet state requires an electron to flip its spin, since the only energetically permitted final state for autodetachment is the ground state of He, which is a singlet state. In addition, the (1s2s2p) ^4P state is metastable against radiative decay since it is the lowest lying state of quartet multiplicity.

Fig. 5.1 is an energy level diagram of the lowest lying states of He and He^-. The ($1s^22s$) ^2S ground state of He^- is unbound. The only long–lived state of He^- is the (1s2s2p) ^4P state. The electron affinity of the parent atomic state He(1s2s) ^3S has been both experimentally [8], [72] and theoretically [22] determined. The currently accepted value is $E_a(He^3S) = 0.07745$ eV. The excitation energy of the He(1s2p) ^3P state above the He(1s2s) ^3S state is well known from optical spectroscopy to be 1.1449 eV [61]. The rather small fine structure splittings of He^-(1s2s2p) ^4P_J were determined using a radiofrequency resonance technique [73]. The J=5/2-1/2 and 5/2-3/2 separations were found to be 3.581 x 10^{-5} eV and 3.411 x 10^{-6} eV, respectively. Blau et al. [74] measured the lifetimes of the J=5/2,3/2 and 1/2 levels of the (1s2s2p) ^4P state to be 500 $\pm$ 100 μs, 10 $\pm$ 2 μs and 16 $\pm$ 4 μs, respectively. The differential metastability is a result of the different strengths of the magnetic interactions that induce autodetachment. The total cross section for photoejecting electrons from He^-(1s2s2p) ^4P has been measured by Compton et al. [42] and Peterson et al. [75] for visible wavelengths. Hazi and Reed [76] reported the results of a calculation of the total cross section for the photodetachment of He^- for photon energies up to 2.75 eV above the He^-(1s2s2p) ^4P state.

In the present thesis, the first measurements of the angular distributions of electrons produced in the photodetachment of He^- are described. The two competing exit channels were energetically resolved. The spectral dependences

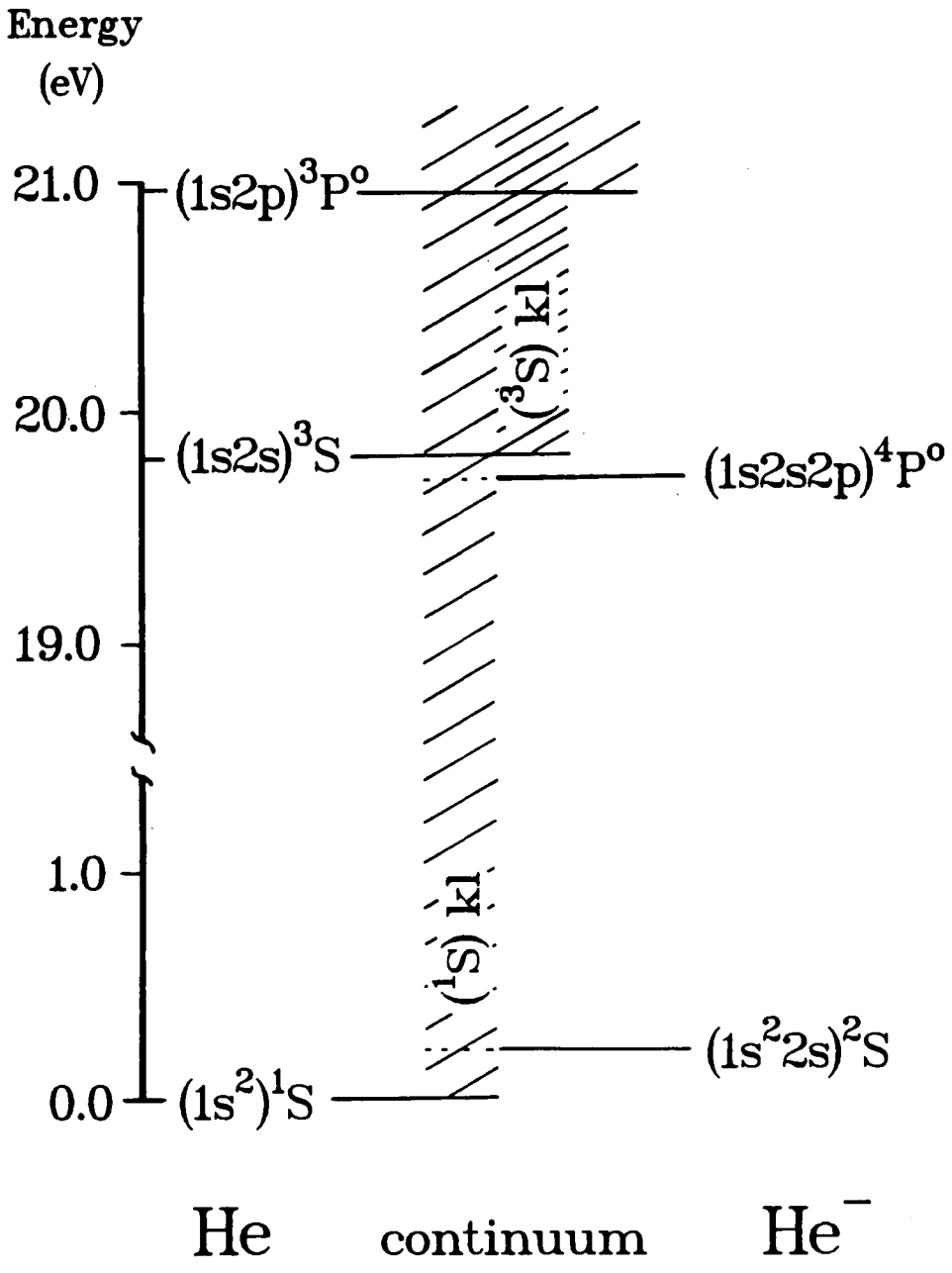


Figure 5.1: Partial energy level diagram of He and He^-

of the asymmetry parameters characterizing the angular distributions of the electrons photodetached in these channels have been measured over a range of photon energies from 1.775 to 2.456 eV.

5.2 Energy– and Angle–Resolved Measurements

The energy– and angle–resolved measurements described in this chapter were made with the crossed–beams apparatus described in Chapter 3. In the case of the He^- measurements, the ions were produced by passing He^+ ions, in the energy range of 20 to 40 keV, through a lithium vapor cell. The He^- beam current monitored at the Faraday cup positioned behind the electron spectrometer was typically ~0.02 nA. The negative ion beam was crossed with a linearly–polarized and energy–resolved photon beam from a flashlamp–pumped dye laser just prior to the entrance of the electron spectrometer.

A spectrum of the number of photoelectrons versus their laboratory kinetic energy was obtained by ramping the voltage on the entrance aperture of the spectrometer. The voltage was incremented, in this case, in steps of ~0.048 V. The electron spectrometer was operated in a fixed pass–energy mode. The background electron signal associated with processes other than photodetachment was subtracted from the photoelectron signal in the manner described in Section 3.5. Signals proportional to the instantaneous ion and photon beam intensities were also recorded so that the photoelectron signal could be normalized to fluctuations in the intensities of these beams.

The experiment described in this chapter was designed so that the negative ion and photon beams crossed perpendicularly. The electron spectrometer was placed in the path of the negative ion beam so that it collected only these photoelectrons ejected in the forward direction in the laboratory frame (see Fig. 3.3). In this geometry the angular correlation factor, $f(\theta)$, for electrons photodetached

by linearly polarized light is described by Eq. 5.2. In general, kinematics will rotate the photoelectron emission pattern as measured in the laboratory frame with respect to that in the ion frame. However, for the special case of forward–directed electron spectroscopy that has been used in these experiments, this kinematic rotation effect is reduced to zero (see Section A.4).

The angular distribution of the electrons photodetached from He^- was investigated by taking electron energy spectra at various angles between the photoelectron emission direction and the linear polarization vector of the laser beam. The angle was changed by rotating the polarization vector relative to the fixed photoelectron collection direction. The spectral dependence of the asymmetry parameter was determined by studying the emission pattern of the electrons at various photon energies. The photon energy was varied by frequency tuning the output of the dye laser.

Fig. 5.2 shows an energy spectrum of the electrons ejected from He^- following photodetachment. The ion beam energy in this case was 40 keV and the photon wavelength was 698.5 nm (E_γ = 1.775 eV). Peaks 1 and 2 are the backward– and forward–directed peaks, respectively, corresponding to the channel $He^-(1s2s2p)\ ^4P + h\nu \longrightarrow He(1s2p)\ ^3P + e^-(kp)$. Peak 3 is the forward–directed peak that corresponds to the channel $He^-(1s2s2p)\ ^4P + h\nu \longrightarrow He(1s2s)\ ^3S + e^-(ks,d)$. This spectrum was accumulated with the electric field vector of the linearly–polarized laser beam directed toward the entrance aperture of the spectrometer (i.e. $\theta = 0°$). Notice that the two forward–directed peaks are well separated in energy. Since the peaks are resolved in energy, it was possible to determine separately the asymmetry parameters for both the $(1s2s)\ ^3S$ and $(1s2p)\ ^3P$ exit channels. Here the photodetachment channels are labeled by the final state of the residual atom. In all cases the resolution of the electron spectrometer was insufficient to separate the fine structure components of the spectral peaks.

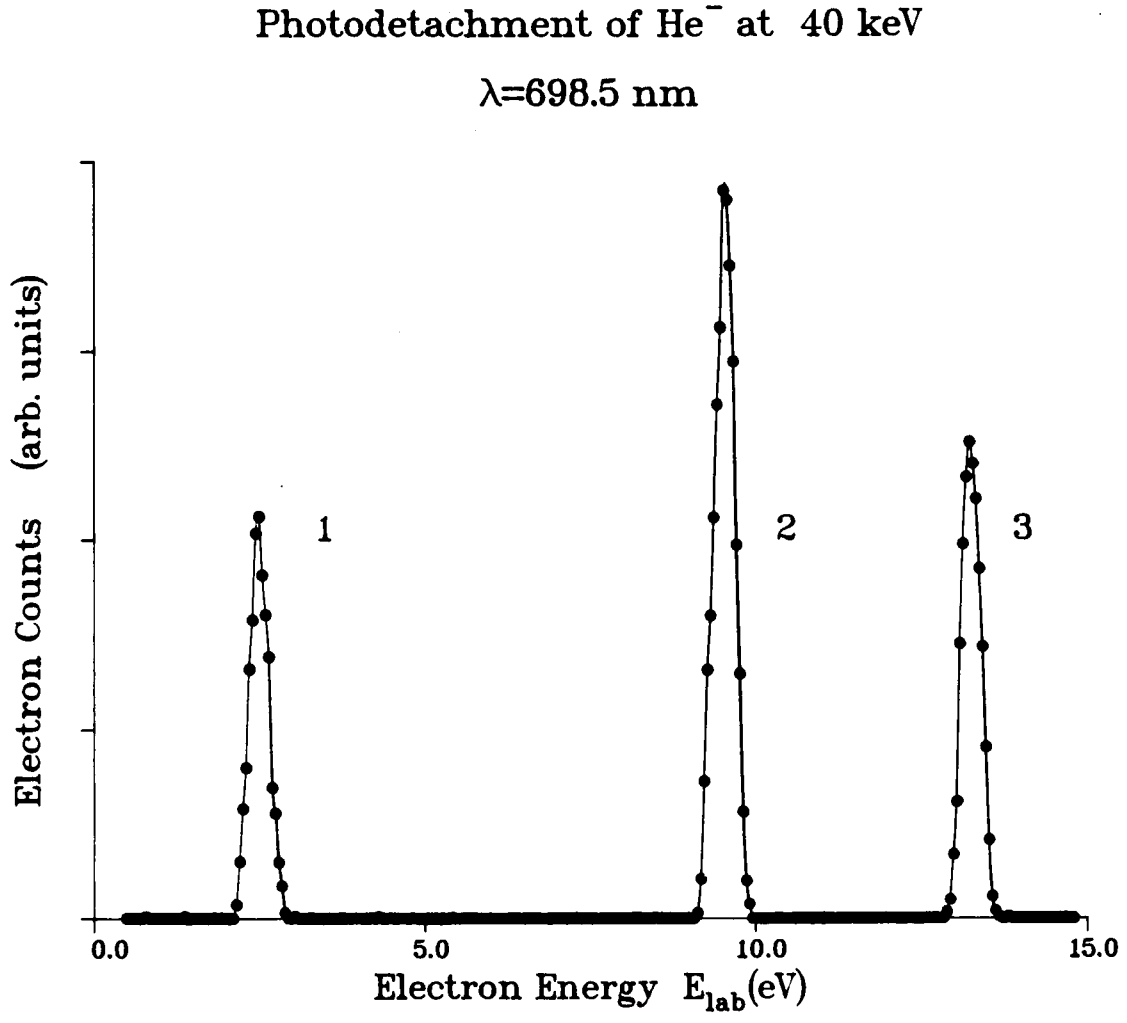


Figure 5.2: A typical kinetic energy spectrum of electrons photodetached from a beam of He^- ions. Peaks 1 and 2 are associated with the photodetachment channel that leaves the He atom in the ^3P state. Peak 3 corresponds to the photodetachment channel that leaves the He atom in the ^3S state.

The electron affinity of He can also be determined from analysis of photoelectron energy spectra. A measurement of the separations of peaks 1 and 2 and peaks 2 and 3 allows one to determine the electron affinity without a need to know the ion beam energy. The same technique was used to measure the electron affinity of Ca, as described in Section 4.3.1. The electron affinity of He(1s2s) ^{3}S was measured to be $E_a(He) = 0.076 \pm 0.003$ eV. This measurement, although not as accurate as the accepted value [22], [72], is otherwise in good agreement with it. This single measurement was used to test the technique that has been developed to determine electron affinities via kinematic peak shifting and doubling. The uncertainties could be reduced considerably by accumulating more data sets.

The photoelectron yield (the area under the peak) is proportional to the differential cross section for ejecting an electron from He^-. The total partial cross section for photodetachment is constant at a particular photon energy, and therefore

$$Y(\theta) \propto 1 + \beta P_2(\cos\theta), \tag{5.3}$$

where $Y(\theta)$ is the photoelectron yield at a known angle θ. The photoelectron yield was determined by fitting the data points associated with each peak to a gaussian function by the method of weighted least–squares [63]. Each data point was statistically weighted in the fit. The fitting parameters were the height, full width at half–height and the centroid of the gaussian function. Errors were assigned to the fitting parameters corresponding to the goodness of the fit. The area of the peak was then determined by using Simpson's method [77] to numerically integrate a gaussian function. The parameters used to find the area were those determined by the fitting procedure.

Fig. 5.3 is a plot of the photoelectron yield versus θ for the photodetachment process $He^-(1s2s2p)\ ^4P + h\nu \longrightarrow He(1s2p)\ ^3P + e^-(k,p)$. The photon wavelength was 638.4 nm ($E_\gamma = 1.942$ eV). The solid line is a least–squares fit to

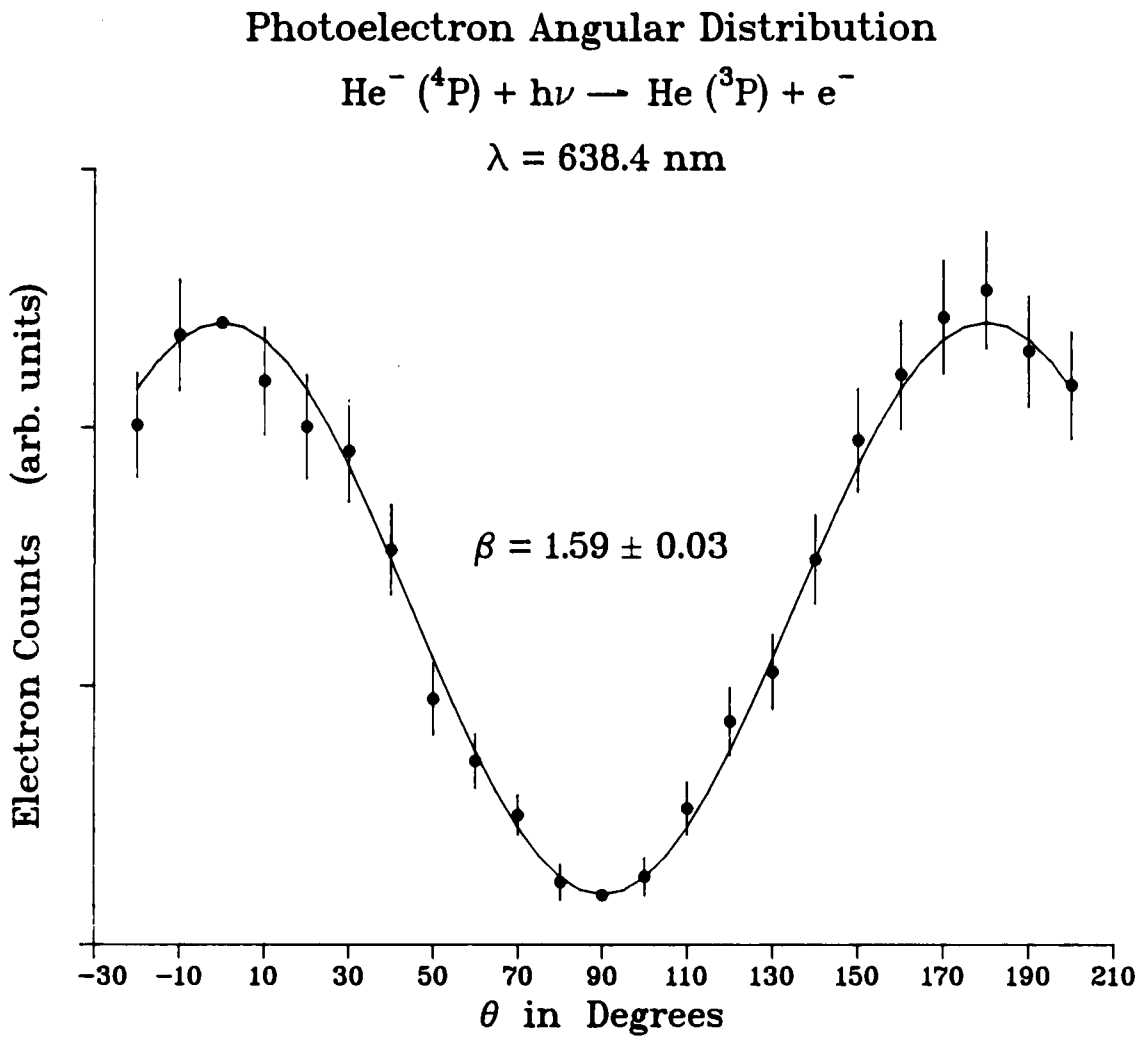


Figure 5.3: Angular dependence of the photoelectron yield for the ^3P exit channel

the function $1 + \beta P_2(\cos\theta)$, where β is treated as the fitting parameter. In this case $\beta = 1.59 \pm 0.03$. The laboratory frame angular resolution for these angular distribution studies was 1.4°. This data served to calibrate the angle scale for the emission pattern measurements.

Once the angle scale has been established, a simpler method of determining β, and the one primarily used in this thesis, is to measure the photoelectron yield at two known values of θ. In this case $\theta = 0°$ and 90° were chosen. The asymmetry parameter was determined by substituting the measured photoelectron yields at two different angles into Eq. 5.3 and taking the ratio of the yields. Thus, the equation used to determine β is

$$\beta = \frac{Y(0°) - Y(90°)}{\frac{1}{2}Y(0°) + Y(90°)}. \tag{5.4}$$

Here Y(0°) and Y(90°) are the measured photoelectron yields at $\theta = 0°$ and 90°, respectively.

5.3 Photoelectron Asymmetry Parameters

5.3.1 Introduction

The apparatus was first tested by studying the angular distribution of electrons photodetached from a beam of negative ions with a known asymmetry parameter. The negative deuterium ion, D^-, for example, is formed in the $(1s^2)\ ^1S$ state and the photodetachment process will leave the residual D atom in the $(1s)\ ^2S$ ground state for all photon energies used in this experiment. In such a light system, spin–dependent interactions are negligibly small. Correlation effects in the $(1s^2)\ ^1S$ state are sufficiently small that they have little effect on the emission process. The angular momentum transferred in this process is zero [78]. The electrons photodetached from D^- should therefore be pure p–wave electrons and they will carry off the full anisotropy of the photon–D^- interaction. The angular

distribution of photoelectrons for such an independent electron interaction should follow a $\cos^2\theta$ emission pattern, characterized by $\beta = 2$. The asymmetry parameter for electrons photodetached from D^- was measured in this work to be $2.00\ ^{+0.00}_{-0.03}$ for $E_\gamma = 2.224$ eV and $2.00\ ^{+0.00}_{-0.03}$ for $E_\gamma = 1.775$ eV. The photoelectron asymmetry parameter of a similar system, Li^-, was measured to be 1.99 ± 0.01 for $E_\gamma = 2.087$ eV. In each case the measurement was in good agreement with the predictions of the independent electron model (see Section 2.2). As was mentioned in the previous section, the laboratory frame angular resolution for these measurements was 1.4°. A correction to the photoelectron yields for the finiteness of the angular resolution was found to be negligibly small in all the measurements described in this thesis.

One of the assumptions made in order for the angular correlation factor, $f(\theta)$, to have the form $1 + \beta P_2(\cos\theta)$, was that the magnetic substates of the negative ion are all equally populated prior to photoabsorption. It is to be expected that the alignment of the orbital angular momentum vector in the $He^-(1s2s2p)\ ^4P$ state produced in the double charge transfer production process will be small. Even if there were some alignment induced in the production process it would almost certainly be "averaged out" during the time of flight of the ions to the interaction region. This flight time is much longer than the spin–orbit precessional period associated with the fine structure levels. The coupling of aligned orbital angular momentum vectors to randomly–oriented spin vectors via the spin–orbit interaction for many precessional periods should be sufficient to randomize the orbital angular momentum vectors by the time the ions reach the interaction region. Thus the magnetic substates should be statistically populated prior to photodetachment.

5.3.2 Asymmetry Parameter for the He(^{3}S) Exit Channel

The asymmetry parameter has been studied for the photodetachment process, $He^-(1s2s2p)\ ^4P + h\nu \longrightarrow He(1s2s)\ ^3S + e^-(ks,d)$, as a function of the incident photon energy using linearly polarized light. Photoelectron yields were measured at the angles $\theta = 0°$ and 90°. The method described in the previous section was used to determine the asymmetry parameters. Approximately ten spectra were recorded for each angle at six different photon energies. The photon energies ranged from 1.775 to 2.456 eV. The individual values of β are shown in Table 5.1.

Fig. 5.4 shows the spectral dependence of the asymmetry parameter for electrons photodetached from He^- via the exit channel that leaves the He atom in the (1s2s) ^{3}S state. The solid line through the data points represents a weighted least–squares polynomial fit. It is only intended to guide the eye.

The photodetachment process $He^-(1s2s2p)\ ^4P + h\nu \longrightarrow He(1s2s)\ ^3S + e^-(ks,d)$ is described by an independent electron model as photoejecting a p–orbital electron leading to outgoing s and d partial waves. According to the Cooper-Zare model [11], the value of β, at any given photon energy, will depend on an interference between the outgoing s and d waves. The asymmetry parameter is sensitive to both the relative magnitudes of the dipole integrals and the phase differences between the two partial waves and will, in general, vary with photon energy (see Section 2.2).

5.3.3 Asymmetry Parameter for the He(^{3}P) Exit Channel

The photoelectron asymmetry parameter for the process $He^-(1s2s2p)\ ^4P + h\nu \longrightarrow He(1s2p)\ ^3P + e^-(kp)$ has been studied as a function of the incident photon energy using linearly polarized radiation. Photoelectron yields were measured at the angles $\theta = 0°$ and 90°. The asymmetry parameter was determined by

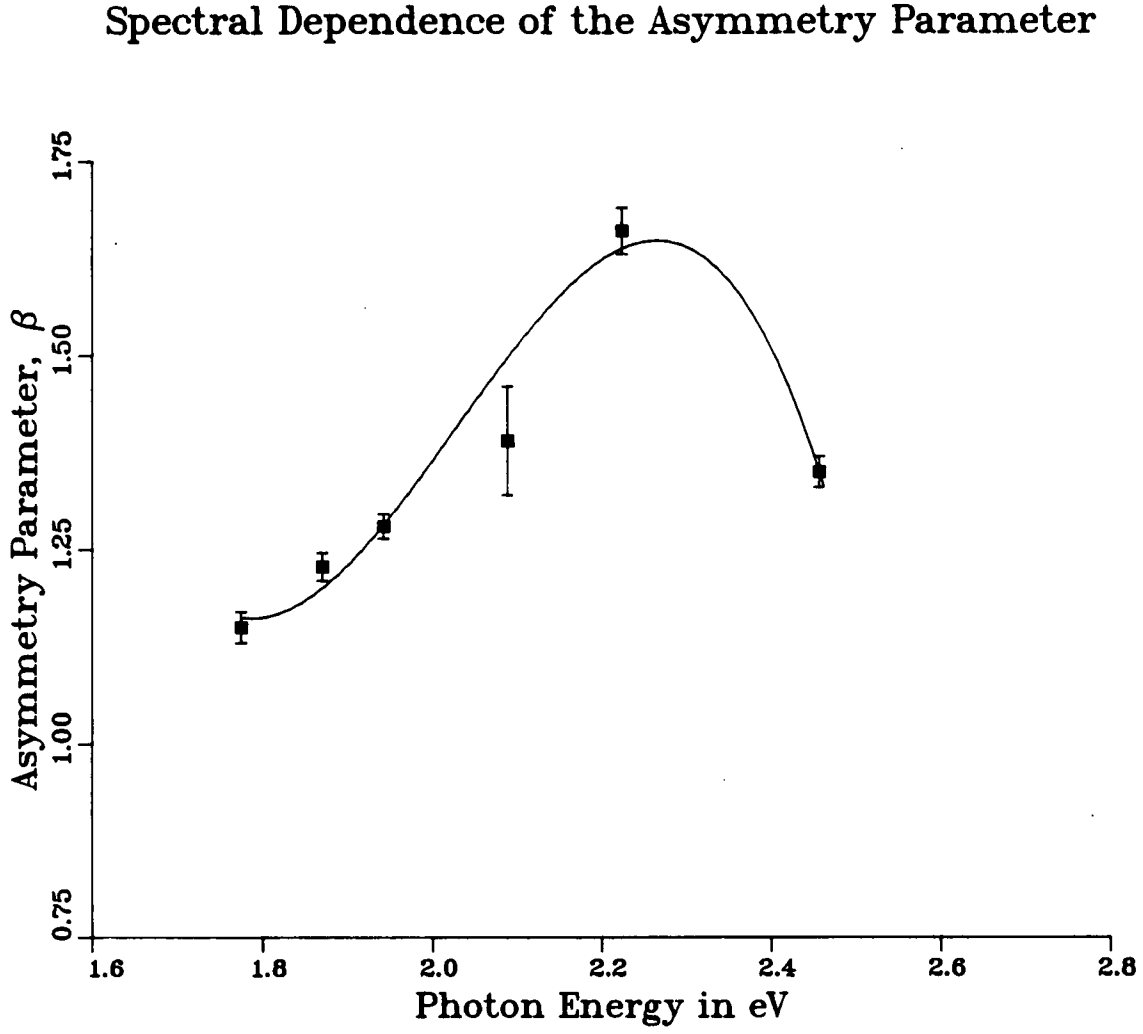


Figure 5.4: Spectral dependence of the asymmetry parameter for electrons photodetached from He^- via the ^3S exit channel

Table 5.1: Asymmetry parameters for the ^{3}S exit channel

E_γ (eV)	β
2.456	1.35 ± 0.02
2.224	1.63 ± 0.05
2.087	1.31 ± 0.07
1.942	1.28 ± 0.02
1.870	1.23 ± 0.02
1.775	1.15 ± 0.02

a method described in Section 5.2. Approximately ten spectra were taken at each angle for six different photon energies. The photon energies ranged from 1.775 to 2.456 eV. The individual β values are shown in Table 5.2.

Fig. 5.5 shows the spectral dependence of the asymmetry parameter for the electrons photodetached in the process which leaves the residual He atom in the (1s2p) ^{3}P state. The solid line through the data points represents a weighted least–squares polynomial fit. It is only intended to guide the eye.

An independent electron model describes photodetachment into the exit channel that leaves the He atom in the (1s2p) ^{3}P state as the photoejection of an s–orbital electron leading to an outgoing electron described by a p–wave. Cooper and Zare's model [11] predicts that $\beta = 2$ for photoejecting an s–orbital electron, independent of the incident photon energy. An independent electron model does not, therefore, describe the observed decrease in β at the lower photon energies. Electron correlation in either the initial or final state must be responsible for the rather dramatic change in the value of the asymmetry parameter within this small range of photon energies.

Bunge [22] calculated the configuration interaction coefficients for the possible configurations contributing to the ^{4}P state of He^-. The 1s2s2p configuration has a mixing coefficient of ~0.98. Thus the ^{4}P state is well described

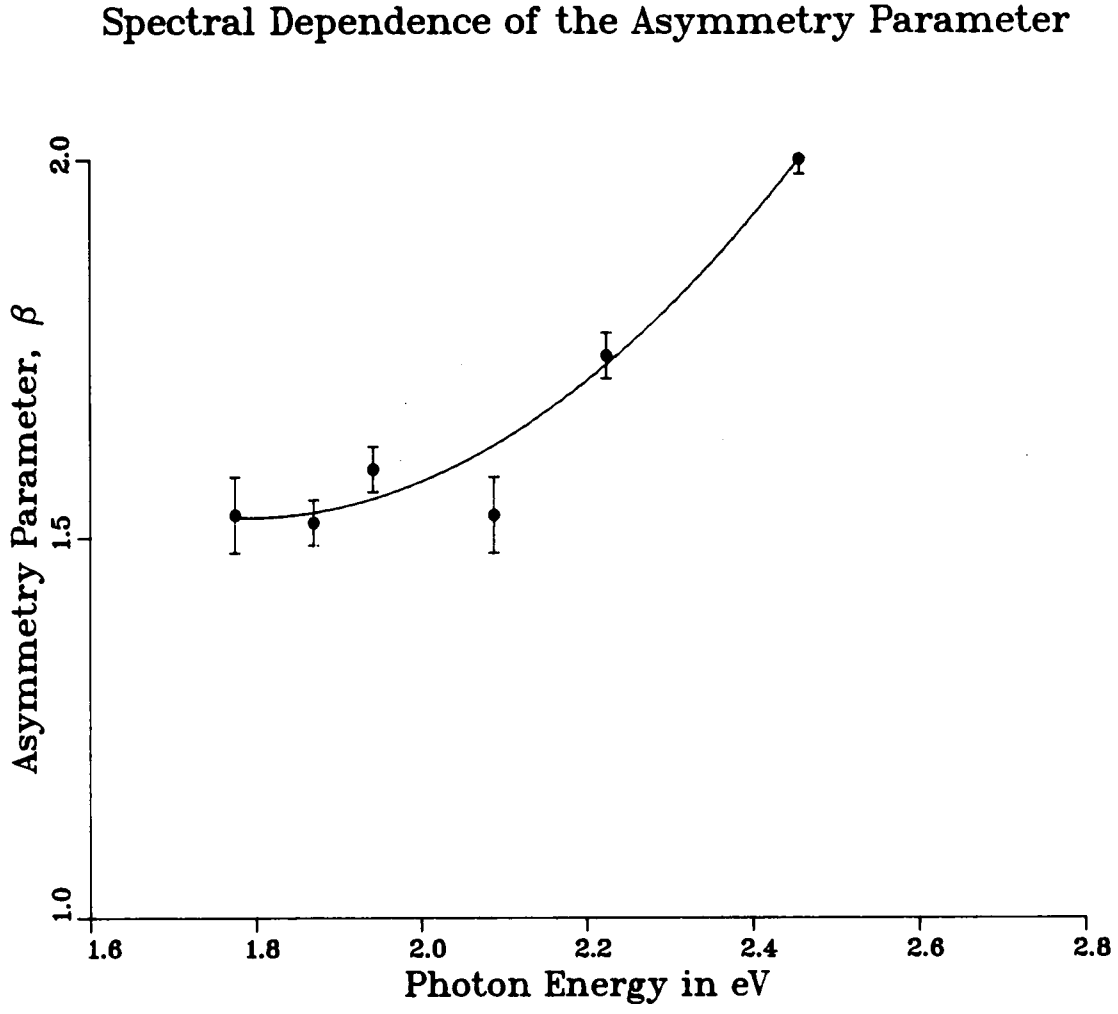


Figure 5.5: Spectral dependence of the asymmetry parameter for electrons photodetached from He^- via the ^3P exit channel

Table 5.2: Asymmetry Parameters for the ^{3}P Exit Channel

E_γ (eV)	β
2.456	$2.00 \pm {}^{0.00}_{0.03}$
2.224	1.74 ± 0.03
2.087	1.53 ± 0.05
1.942	1.59 ± 0.03
1.870	1.52 ± 0.03
1.775	1.52 ± 0.04

by the 1s2s2p configuration. Cooper and Zare [11] have shown that, in cases of configuration interaction, an effective asymmetry parameter can be calculated by weighting the one–electron configuration asymmetry parameters by the square of the configurational mixing coefficients. In the case of He^-, the sum of the squares of the configuration mixing coefficients for configurations other than the 1s2s2p configuration is only $\sim$0.04. Thus correlation in the initial state is insufficient to explain the observed large deviation of β from the prediction of an independent electron model.

Two final state interaction mechanisms offer a possible explanation for the observed deviation of the asymmetry parameter from the predictions of an independent electron model. During the time the ejected photoelectron is under the influence of the field of the residual atom, angular momentum transfers can arise if the residual atom is left in a non–spherical state such as the (1s2p) ^{3}P state of He. This anisotropic interaction is between the orbital motion of the electron and the net orbital motion of the electrons of the residual atom. A dynamic coupling of the respective orbital momenta is produced in this interaction. The coupling can result in angular momentum exchanges between the liberated electrons and the residual atomic core, and as a result only the total angular momentum of the final state is conserved.

The possible total orbital momenta for the final state are the (1s2pkp) ^4P,^4S,^4D states. The final state coupling between the angular momenta of the photoelectron and the atomic electrons can reorient the orbital momentum of the liberated electron. This depolarization can dramatically affect the photoelectron angular distributions as has been shown in photoionization studies [18]. In the case of photoionization, the ejected electron moves in the field of a residual ion whereas in photodetachment the electron interacts with a residual atom. In the case of the (1s2p) ^3P state of He, the dominant electrostatic moment is expected to be the quadrupole moment which, in principle, could exert a "torque" on the outgoing electron. The permanent and induced dipole moments for this non-hydrogenic system are expected to be considerably smaller.

Another final state interaction that can result in a spectral deviation in β from the Cooper-Zare model is the photoejection of an electron via a resonance. The photoelectron angular distribution can be changed by an exchange of angular momentum in the protracted, anisotropic electron–atom interaction associated with a resonance state [19]. In such cases in photoionization, the asymmetry parameter has been observed to vary markedly with photon energy across a resonance in the cross section [38]. A resonance in β can, in fact, be an even more pronounced spectral feature than a resonance in the cross section. The cross section depends only on the squared moduli of the scattering amplitudes used to describe the final state interaction, whereas the asymmetry parameter depends on both the moduli and phases of these amplitudes.

There exists a shape resonance in the He^- photodetachment cross section that could possibly be responsible for the observed spectral deviation in β. The (1s2p^2) $^4P^e$ shape resonance was recently studied experimentally by Peterson et al [72] and theoretically by Hazi and Reed [76] and Watanabe [79]. This resonance lies ~11 meV above the (1s2p) ^3P threshold and has a half–width of ~7 meV. The

peak cross section was calculated to be $\sim 8 \times 10^{-15}$ cm^2. The spectral range of the present investigation is approximately one hundred half-widths from the peak in the cross section. Even so far in the wings of the resonance, the cross section has been calculated to be as large as $\sim 10^{-17}$ cm^2 [79]. This resonant cross section is comparable in magnitude to a typical cross section for direct (non-resonant) photodetachment.

It is important to note that the photon-negative ion interaction for the resonant process is inherently anisotropic. The photoexcitation process is necessarily state selective as a result of the use of linearly polarized incident radiation and the restriction imposed on the possible final states by the Pauli exclusion principle. The electrons subsequently ejected in the autodetachment of this resonance will carry away the anisotropy. The emission pattern, in this case, will be characterized by a value of $\beta = 0.5$ [80]. One intriguing possibility is that the shape of the spectral deviation of β observed is the photodetachment of He^- via the ^3P exit channel arises from an interference between direct and resonant photodetachment pathways to the common (1s2pkp) ^4P final state. The measured value of β at any particular photon energy would, in this model, be the result of an appropriate weighting of the β's from the two different pathways. These weighting factors, which will be determined by the relative cross sections for the two interfering processes, are expected to change as a function of the incident photon energy.

5.4 Error Analysis

The measurements of the asymmetry parameters were made by determining the electron yield for a photodetachment process at two different values of the angle θ. The error analysis is completely dominated by the inherent uncertainties in determining the area of the two photoelectron peaks. In the present case,

uncertainties due to counting statistics caused a ~2–4% error in the measurement of each of the two photoelectron yields. Applying standard propagation–of–error analysis [63] to Eq. 5.4 shows that these uncertainties in measuring the photoelectron yield, in turn, produce an uncertainty in β of ~4-8%, as shown by the error bars in Figures 5.4 and 5.5 and Tables 5.1 and 5.2.

5.5 Conclusion

The $He^-(^4P) + h\nu \longrightarrow He(^3S) + e^-$ and $He^-(^4P) + h\nu \longrightarrow He(^3P) + e^-$ photodetachment channels were energetically resolved by the technique of photoelectron detachment spectroscopy. The emission pattern of the photoelectrons in each case was studied by rotating the electric field vector of the linearly–polarized laser light relative to the fixed photoelectron collection direction, and measuring the yield of electrons at each angle. The spectral dependence of the asymmetry parameters was investigated over the photon energy range from 1.775 to 2.456 eV.

The shape of the spectral dependence of β for the ^3S exit channel should be explainable in terms of the changing interference between the s and d partial waves with a possible contribution from a final state interaction. Even in the independent electron model, without considering final state interactions, the value of β is expected to vary as a function of the incident photon energy. No resonances exist in this channel to complicate the theoretical analysis.

The asymmetry parameter for the ^3P exit channel also has a very definite shape over this spectral range. The value of β drops from 2 to ~1.5 as the photon energy decreases. Interelectronic interactions in the initial state are not considered to be sufficiently large to account for the observed effect. In the independent electron model, the value of β is predicted to be constant across the spectral range. Deviations must therefore be associated with a breakdown of this model. Two different types of final state interactions are proposed that could

possibly be responsible for the relatively large change in β that occurs over such a small spectral range. The present measurement will not, however, allow one to distinguish the relative contributions to the change in β brought about by the direct final state interaction and the interaction associated with the presence of the shape resonance.

The data were taken over a somewhat limited spectral range, but even so, the measured asymmetry parameters vary considerably. At the present time, the features in the β spectra do not lend themselves to simple explanations. As yet there has not been a theoretical investigation of the He^- photodetachment process that explains the observed behavior of the asymmetry parameters characterizing the angular distributions of the photoelectrons.

BIBLIOGRAPHY

BIBLIOGRAPHY

[1] H.S.W. Massey and D.R. Bates, Astrophys. J **91**, 202 (1940).

[2] B. Warner, Mon. Not. Roy. Astr. Soc. **137**, 119 (1967).

[3] P.A. Strittmatter and D.T. Wickramasinghe, Mon. Not. Roy. Astr. Soc. **152**, 47 (1971).

[4] Sir Harrie Massey, **Negative Ions**, Cambridge University Press, Cambridge, England, 1976.

[5] L.M. Branscomb and W.L. Fite, Phys. Rev. **93**, A651 (1954).

[6] H. Hotop and W.C. Lineberger, J. Phys. Chem. Ref. Data **14**, 731 (1985).

[7] A. Einstein, Ann. Phys. (Leipzig) **17**, 132 (1905); **20**, 199 (1906).

[8] B. Brehm, M.A. Gusinow and J.L. Hall, Phys. Rev. Lett. **19**, 737 (1967).

[9] H. Hertz, Ann. Phys. (Leipzig) **31**, 983 (1887).

[10] P.G. Burke, **Atomic Processes and Applications**, P.G. Burke and B.L. Moiseiwitsch, Ed., North–Holland Pub. Co., 1976, pp. 242–290.

[11] J. Cooper and R.N. Zare, **Lectures in Theoretical Physics**, S. Geltman, K.T. Mahanthappa and W.E. Brittin, Ed., Gordon and Breach, New York, 1969, Vol. XI–C, pp. 317–337.

[12] Hans A. Bethe, **Intermediate Quantum Mechanics**, W.A. Benjamin, Inc., New York, 1964.

[13] C.L. Perkeris, Phys. Rev. **112**, 1649 (1958); **126**, 1470 (1962).

[14] Kenneth Smith, **The Calculation of Atomic Collision Processes**, Wiley–Interscience, New York, 1971.

[15] Stephen Gasiorowicz, **Quantum Physics**, John Wiley & Sons, New York, 1974.

[16] C.N. Yang, Phys. Rev. **74**, 764 (1948).

[17] U. Fano and Dan Dill, Phys. Rev. A **6**, 185 (1972).

[18] Dan Dill, Anthony F. Starace and Steven T. Manson, Phys. Rev. A **11**, 1596 (1975).

[19] Dan Dill, Phys. Rev. A **7**, 1976 (1973).

[20] H. Hotop and W.C. Lineberger, J. Phys. Chem. Ref. Data **4**, 539 (1975).

[21] A.W. Weiss, Phys. Rev. **122**, 1826 (1961).

[22] Annik Vivier Bunge and Carlos F. Bunge, Phys. Rev. A **19**, 425 (1979).

[23] J.S. Sims, S.A. Hagström, D. Munch and C.F. Bunge, Phys. Rev. A **13**, 560 (1976).

[24] G.D. Alton, T.J. Kvale, R.N. Compton, D.J. Pegg and J.S. Thompson, Nucl. Instru. and Meth. **A244**, 142 (1986).

[25] T.J. Kvale, G.D. Alton, R.N. Compton, D.J. Pegg and J.S. Thompson, Phys. Rev. Lett. **55**, 484 (1985).

[26] T.J. Kvale, R.N. Compton, G.D. Alton, J.S. Thompson and D.J. Pegg, Phys. Rev. Lett. **56**, 592 (1986).

[27] T.J. Kvale, G.D. Alton, R.N. Compton, J.S. Thompson and D.J. Pegg, Nucl. Instru. and Meth. **B24/25**, 325 (1986).

[28] General Ionex Corporation, Newburyport, MA 01950

[29] B.L. Donnally and G. Thoeming, Phys. Rev. **159**, 82 (1967).

[30] B.A. D'Yachkov and V.I. Zinenko, Sov. Phys. Tech. Phys. **16**, 305 (1971).

[31] R.M. Ennis Jr, D.E. Schechter, G. Thoeming, D.B. Schflake, and B.L. Donnally, IEEE Trans. Nucl. Sci. **NS–14**, 75 (1967).

[32] R.J. Girnius and L.W. Anderson, Nucl. Instru. and Meth. **137**, 373 (1976).

[33] A.S. Schlacter, D.H. Loyd, P.J. Bjorkholm, L.W. Anderson and W. Haeberli, Phys. Rev. **174**, 201 (1968).

[34] John H. Moore, Christopher C. Davis and Michael A. Coplan, **Building Scientific Apparatus**, Addison–Wesley Publishing Company, London, 1983.

[35] F.W. Aston, Phil. Mag. **38**, 710 (1919).

[36] E.M. Purcell, Phys. Rev. **54**, 818 (1938).

[37] K. D. Sevier, **Low Energy Electron Spectrometry**, Wiley–Interscience, New York, 1972.

[38] Joseph Berkowitz, **Photoabsorption, Photoionization, and Photoelectron Spectroscopy**, Academic Press, New York, 1979.

[39] Herbert Goldstein, **Classical Mechanics**, p. 86, Addison–Wesley Publishing Company, Reading, Massachusetts, 1981.

[40] N.F. Barber, Proc. Leeds Phil. Lit. Soc. Sci. Sect. **2**, 427 (1933).

[41] C. Feigerle, Ph.D. Thesis, University of Colorado, 1983.

[42] R.N. Compton, G.D. Alton and D.J. Pegg, J. Phys. B **13**, L651 (1980).

[43] B.M. Smirnov, **Negative Ions**, McGraw–Hill, New York, 1982.

[44] H.A. Kurtz and Y. Ohrn, Phys. Rev. A **19**, 43 (1979).

[45] J.F. McNutt and C.W. McCurdy, Phys. Rev. A **27**, 132 (1983).

[46] P.D. Burrow and J. Comer, J. Phys. B. **8**, L92 (1975); P.D. Burrow, J.A. Michejda, and J. Comer, J. Phys. B **9**, 3225 (1976).

[47] H.A. Kurtz and K.D. Jordan, J. Phys. B **14**, 4361 (1981).

[48] E. Heinicke, H.J. Kaiser, R. Rockwitz and D. Feldman, Phys. Lett. **50A**, 265 (1974).

[49] A.W. Weiss, Phys. Rev. **166**, 70 (1968).

[50] C.F. Bunge, M. Galan, R. Jaurequi and A.V. Bunge, Nucl. Instru. and Meth. **202**, 299 (1982).

[51] D.J. Pegg, Book of Abstracts, DOE Atomic Physics Contractors Workshop, 1985, p. 8.

[52] G. Aspromallis, C.A. Nicolaides and D.R. Beck, J. Phys. B **19**, 173 (1986).

[53] Donald R. Beck, Phys. Rev. A **30**, 3305 (1984).

[54] Donald R. Beck, private communication.

[55] J. Heinemeier and P. Hvelplund, Nucl. Instru. and Meth. **148**, 425 (1975).

[56] D.J. Pegg, J.S. Thompson, R.N. Compton and G.D. Alton, Phys. Rev. Lett. **59**, 2267 (1987).

[57] C. Froese Fischer, J.B. Lagowski and S.H. Vosko, Phys. Rev. Lett. **59**, 2263 (1987).

[58] P. Krylstedt, N. Elander and E. Brändas, J. Phys. B (to be published).

[59] C. Feigerle, Ph.D. Thesis, p. 10, University of Colorado, 1983.

[60] P.C. Engelking and W.C. Lineberger, Phys. Rev A **19**, 149 (1979).

[61] **Atomic Energy Levels, Vol. I, ^{1}H–^{23}V**, edited by C.E. Moore, NSRDS–NBS35, 1971.

[62] C.S. Feigerle, R.R. Corderman and W.C. Lineberger, J. Chem. Phys. **74**, 1513 (1981).

[63] Philip R. Bevington, **Data Reduction and Error Analysis for the Physical Sciences**, McGraw–Hill, New York, 1969.

[64] C.W. Clark, private communication.

[65] C. Froese Fischer, private communication.

[66] J.L. Hall and M.W. Siegel, J. Chem. Phys. **48**, 943 (1968).

[67] J. Cooper and R.N. Zare, J. Chem. Phys. **48**, 942 (1968).

[68] A. Kasdan and W.C. Lineberger, Phys. Rev. A **10**, 1658 (1974).

[69] D.L. Moores and D.W. Norcross, Phys. Rev. A **10**, 1646 (1974).

[70] J.W. Hiby, Ann. Phys. (Leipzig) **34**, 473 (1979).

[71] E. Holøien and J. Mitdal, Proc. Phys. Soc. London A **68**, 815 (1955).

[72] J.R. Peterson, Y.K. Bae and D.L. Huestis, Phys. Rev. Lett. **55**, 692 (1985).

[73] D.L. Mader and R. Novick, in **Atomic Physics 3**, S.J. Smith and G.K. Walters, Ed., Plenum, New York, 1973, p. 169.

[74] L.M. Blau, R. Novick and D. Weinflash, Phys. Rev. Lett. **24**, 1268 (1970).

[75] R.V. Hodges, M.J. Coggiola and J.R. Peterson, Phys. Rev. A **23**, 59 (1981).

[76] A.U. Hazi and K. Reed, Phys. Rev. A **24**, 2269 (1981).

[77] V.A. Dyck, J.D. Lawson and J.A. Smith, **Introduction to Computing**, p. 150, Reston Publishing Company, Inc., Reston, Virginia, 1979.

[78] Steven T. Manson and Anthony F. Starace, Revs. of Mod. Phys. **54**, 389 (1982).

[79] Shinichi Watanabe, Phys. Rev. A **25**, 2074 (1982).

[80] J. Burgdörfer, private communication.

[81] N. Stolterfoht, Physics Reports **146**, 317 (1987).

[82] J.D. Jackson, **Classical Electrodynamics**, p. 522, John Wiley & Sons, New York, 1975.

APPENDIX

APPENDIX

A.1 Introduction

The source of negative ions used in this this study of photon–negative ion collisions is a fast moving ion beam. The ion reference frame is moving relative to the laboratory reference frame. The physical quantities of interest are associated with the ion frame, but the measurements are made in the laboratory frame. A set of equations must be used to transform the laboratory frame measurements into the quantities that correspond to the physics in the ion frame. Stolterfoht [81] has described the various kinematic effects encountered in electron spectroscopy of fast moving beams.

A.2 Transformation of Kinetic Energies and Angles

One of the quantities of interest in the experiment is the kinetic energy of an electron ejected during a photon–ion collision. The photoelectrons are collected and energy analyzed. To obtain a spectrum, the number of electrons is monitored as a function of their laboratory kinetic energy (E_l). The kinetic energy, E_l, must be transformed into the kinetic energy of the electron in the ion frame, E_c, before the knowledge of the electron's kinetic energy can be used, for example, to determine the structure of a negative ion.

Consider an ion beam traveling along the z–axis. Fig. A.1 shows the velocity vectors and the angles relative to the z–axis of an electron ejected in flight by an ion in the beam, for both the ion and laboratory reference frames. The velocity vector, $\vec{v_c}$, represents an electron ejected with a speed $\mid \vec{v_c} \mid$ at an angle θ_c relative to the z–axis in the ion frame. The ion is traveling with the beam velocity, $\vec{v_i}$, parallel to the z–axis. Adding $\vec{v_i}$ and $\vec{v_c}$ gives the velocity vector $\vec{v_l}$ for an electron ejected at an angle θ_l relative to the z–axis in the laboratory frame. With this choice of coordinate frames, the angles that the velocity vectors make with respect to the x–axis in the x–y plane are equal ($\phi_c = \phi_l$) for both the laboratory and ion frames.

The projections of $\vec{v_l}$ and $\vec{v_c}$ on the x–y plane are equal,

$$v_c \sin\theta_c = v_l \sin\theta_l \tag{A.1}$$

and the relationship between the projections of $\vec{v_l}$ and $\vec{v_c}$ on the z–axis is

$$v_c \cos\theta_c = v_l \cos\theta_l - v_i. \tag{A.2}$$

An equation can be derived that transforms the ion frame angle θ_c into the laboratory angle θ_l. Dividing Eq. A.1 by Eq. A.2 leads to

$$\tan\theta_c = \frac{\sin\theta_l}{\cos\theta_l - v_i/v_l}. \tag{A.3}$$

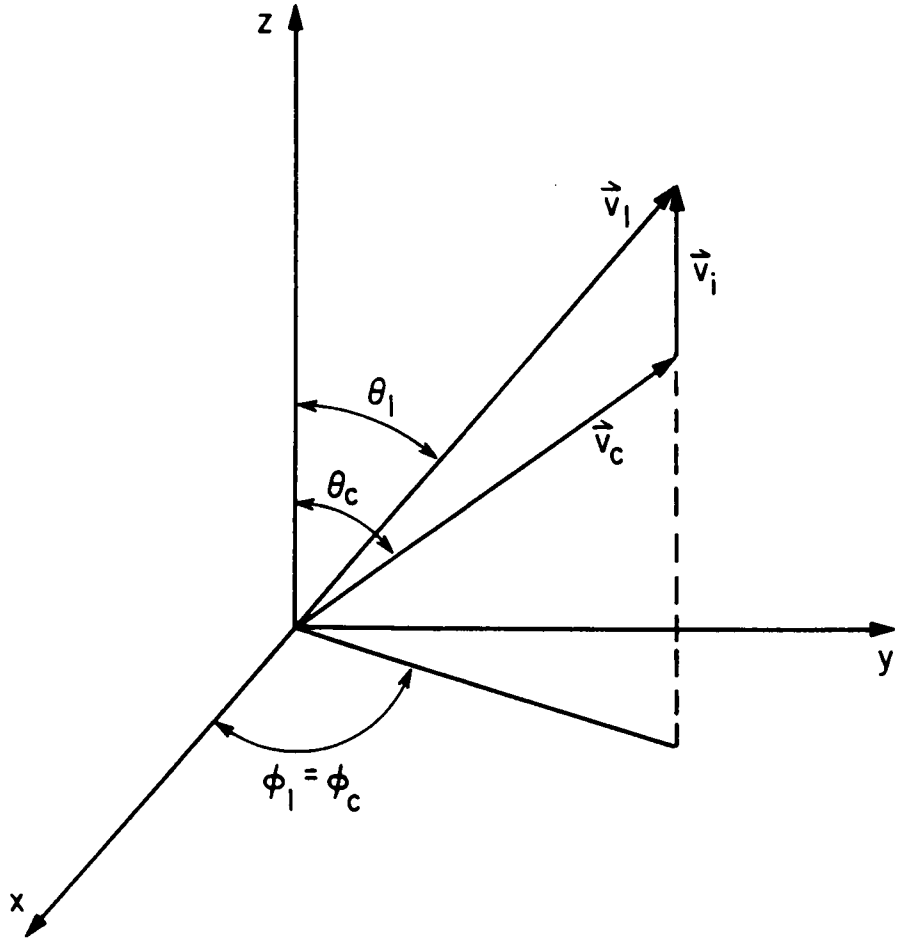


Figure A.1: Transformation from laboratory rest frame to ion rest frame

Notice that for $\theta_l = 0°$, the angle θ_c is double valued, $\theta_c = 0°$ or 180°.

Squaring Eq. A.1 and Eq. A.2 and adding gives

$$v_c^2 = v_l^2 + v_i^2 - 2v_i v_l \cos\theta_l. \tag{A.4}$$

By multiplying Eq. A.4 by $(1/2)m_e$, where m_e is the mass of the electron, an equation is found relating the electron's kinetic energy in the ion frame, E_c, to the corresponding kinetic energy in laboratory frame E_l,

$$E_c = E_l + \epsilon - 2\sqrt{\epsilon E_l}\cos\theta_l, \tag{A.5}$$

where $\epsilon = (1/2)m_e v_i^2 = (m_e/M_i)E_i$. Here E_i and M_i are the kinetic energy and mass of the ion, respectively. The quantity, ϵ, is the kinetic energy of an electron moving with the same velocity as an ion. Solving this quadratic equation for E_l yields

$$E_l = (\sqrt{\epsilon}\cos\theta_l \pm \sqrt{E_c - \epsilon\sin^2\theta_l})^2. \tag{A.6}$$

Eq. A.6 is the transformation equation that relates the kinetic energies of the ejected electron in the laboratory and ion reference frames. Here ϵ and θ_l are laboratory measurable quantities.

In the experiments described in this thesis, the negative ion beam travels through the electron spectrometer (see Fig. 3.3) and the electron collection direction is along the z–axis of Fig. A.1. This limits the laboratory angle, θ_l, to a small range of angles around 0°. Substituting $\theta_l = 0°$ into Eq. A.6 gives

$$E_l = E_c + \epsilon \pm 2\sqrt{\epsilon E_c}. \tag{A.7}$$

The positive sign corresponds to electrons emitted in the positive z direction ($\theta_c = 0°$) and the negative sign to emission in the negative z direction ($\theta_c = 180°$). Notice that for electrons ejected in the forward direction in the ion frame, E_l is always larger than E_c. Experimentally, this kinematic "magnification" allows one to study photodetachment processes producing slow electrons.

When $E_c + \epsilon > 2\sqrt{\epsilon E_c}$ (this is equivalent to $v_i > v_c$), E_l becomes double valued, corresponding to electrons ejected in both the positive and negative z direction. The backward–ejected electrons are "swept" into the electron spectrometer by the velocity of the ion beam. This "kinematic doubling" creates two peaks in the photoelectron spectrum that both originate from the same process.

If the conditions for E_l being double valued are satisfied, an equation can be found that relates the difference between the kinetic energies of the forward and backward–directed electrons to the ion frame kinetic energy, E_c. The difference in energy between the kinematically–doubled pair of peaks will be

$$\Delta E_l = E_l^{\theta_c=0°} - E_l^{\theta_c=180°} = 4\sqrt{\epsilon E_c} \tag{A.8}$$

which can be rearranged to become

$$E_c = \frac{(\Delta E_l)^2}{16\epsilon}. \tag{A.9}$$

This equation indicates a very simple way to find the ion frame kinetic energy of a photoelectron when E_l is double valued (i.e. when $v_i > v_c$) and the reduced ion beam energy, ϵ, is known.

A.3 Transformation of Solid Angle

The kinematic effect of a fast–moving negative ion beam can also be seen in the change of the solid angle of emission for photoelectrons. An equation that relates the solid angle in laboratory frame, $d\Omega_l$, to the corresponding solid angle in the ion frame $d\Omega_c$ is required before photoelectron yields, for example, can be transformed from one frame to another.

In a spherical coordinate system, the ratio of solid angles is given by

$$\frac{d\Omega_l}{d\Omega_c} = \frac{\sin\theta_l d\theta_l d\phi_l}{\sin\theta_c d\theta_c d\phi_c}. \tag{A.10}$$

Fig. A.1 shows that there is cylindrical symmetry about the ion beam vector so that $d\phi_l/d\phi_c = 1$. It is advantageous to find an expression for $d\Omega_l/d\Omega_c$ that involves quantities more readily known than θ_l and θ_c.

Starting with Equations A.1 and A.2, an equation similar to Eq. A.5 can be derived,

$$E_l = E_c + \epsilon + 2\sqrt{\epsilon E_c}\cos\theta_c. \tag{A.11}$$

Taking the derivative of E_l with respect to θ_c gives

$$\sin\theta_c d\theta_c = -2\sqrt{\epsilon E_c} dE_l. \tag{A.12}$$

An equation containing $\sin\theta_l d\theta_l$ can be derived by taking the derivative of E_l with respect to θ_l using Eq. A.5 i.e.,

$$\sin\theta_l d\theta_l = -2\sqrt{\epsilon E_c} dE_c. \tag{A.13}$$

Substituting Equations A.12 and A.13 into Eq. A.10 leads to

$$\frac{d\Omega_l}{d\Omega_c} = \sqrt{\frac{E_l}{E_c}}\frac{dE_l}{dE_c} \tag{A.14}$$

which can be further simplified using Eq. A.11,

$$\frac{d\Omega_l}{d\Omega_c} = \sqrt{\frac{E_l}{E_c}}\left(1 + \sqrt{\frac{\epsilon}{E_c}}\cos\theta_c\right). \tag{A.15}$$

The emission of forward–directed electrons in the ion frame corresponds to the case where $\cos\theta_c = 1$. Solving Eq. A.6 for $\sqrt{\epsilon}$ when $\theta_c = 0°$ and substituting leads to the simple expression,

$$\frac{d\Omega_l}{d\Omega_c} = \frac{E_l}{E_c} = \left(1 + \sqrt{\frac{v_i}{v_c}}\right)^2. \tag{A.16}$$

This equation is particularly useful when transforming the differential cross section measured in the laboratory frame into the ion frame differential cross section, i.e.

$$\left.\frac{d\sigma}{d\Omega}\right|_c = \left.\frac{d\sigma}{d\Omega}\right|_l \left(\frac{d\Omega_l}{d\Omega_c}\right). \tag{A.17}$$

Eq. A.16 provides a simple way to transform differential cross sections using terms that are experimentally easy to measure.

A.4 Rotation of Angular Distributions

In order to transform the measured photoelectron angular distribution into the rest frame of the ion, the effect of the velocity of the ion beam on the angular distribution must be studied. Electrons photodetached by linearly polarized electric dipole radiation are emitted symmetrically about the polarization vector $\hat{\varepsilon}$ (see Section 3.2). In this case, the angular distribution can be written in a form that is a function of the polar angle between the polarization vector and the velocity vector of the emitted electron.

Fig. A.2 shows the velocity vectors and angles that apply to a discussion of the transformation of angular distributions for the geometry of this experiment. The velocity vectors and the angles θ_l and θ_c are described in Section A.2. The experiment is designed so that $\hat{\varepsilon}$ is confined to the x–z plane and the electrons are collected when ejected along the positive z axis. The angle θ' is the angle between $\hat{\varepsilon}$ and $\vec{v_c}$, so the angular distribution in the ion frame is represented by a function $f(\theta')$. The angular distribution in the laboratory frame is in a similarly represented by a function, $g(\theta)$, where θ the angle between $\hat{\varepsilon}$ and the direction of emission of the photoelectron, as measured in the laboratory frame. Inspection of Fig. A.2 indicates a relationship between θ' and θ,

$$\theta = \theta' + \eta \tag{A.18}$$

so that

$$g(\theta) = g(\theta' + \eta). \tag{A.19}$$

The angle η is a phase constant that relates the electron emissions in the ion and laboratory frames. Using the law of sines, an expression for η can be found

$$\eta = \sin^{-1}\left(\frac{v_i}{v_c}\sin\theta_l\right). \tag{A.20}$$

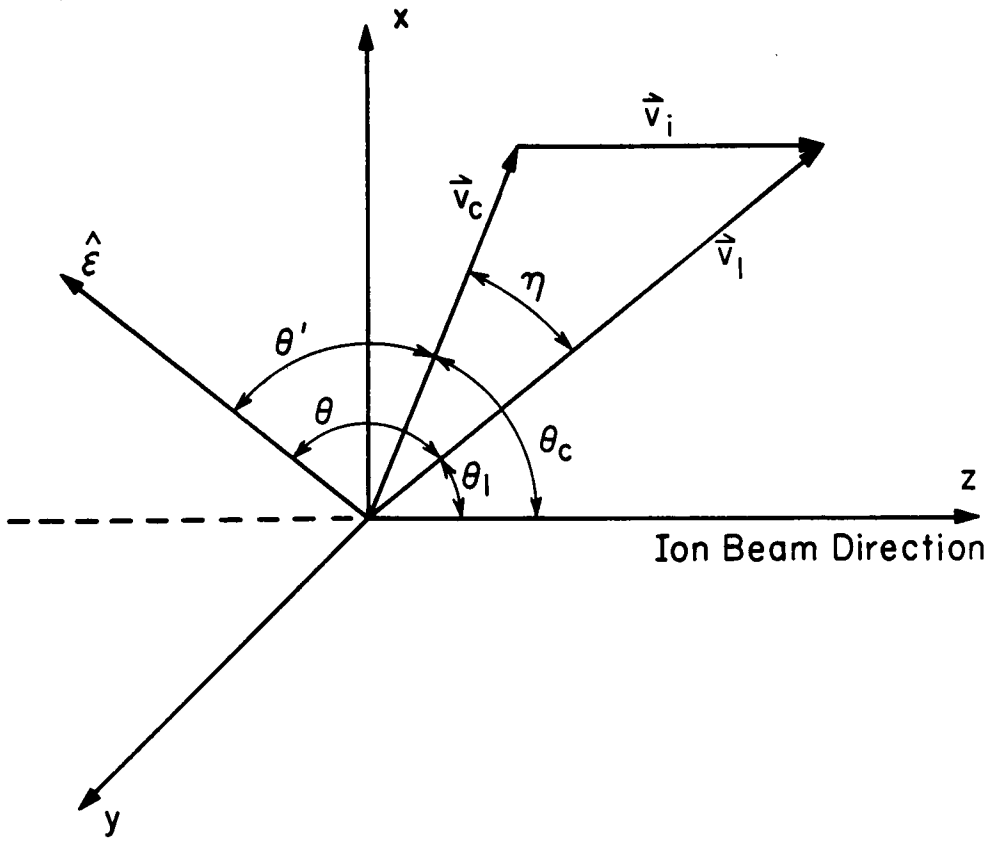


Figure A.2: The effect of kinematics on photoelectron angular distributions

This equation shows that the velocity of the ion beam, in general, rotates the angular distribution by the angle η.

In the geometry of the present experiment, $\theta_l = 0$, so that $\eta = 0$, and $\theta = \theta'$. Eq. A.19 then becomes

$$g(\theta) = g(\theta'). \tag{A.21}$$

This requires that the dependence of $f(\theta')$ on θ' must be the same as $g(\theta)$ on θ. By careful design of the experiment, the measured angular dependence of photoelectron emission is equal to the ion frame angular distribution of photodetached electrons.

A.5 Relativistic and Recoil Effects

Throughout this thesis the corrections for relativistic and ion recoil effects have been assumed to be negligibly small. The velocities of the ions and the photodetached electrons are both less than 1% of the speed of light. Under these circumstances, the relativistic corrections to kinetic energies and velocities are small and the use of classical mechanics is justified.

The frequency of light absorbed by the negative ion, ν_c, is related to the frequency of the light in the laboratory frame, ν_l, by the relativistic Doppler equation [82],

$$\nu_c = \frac{\nu_l(1 - \frac{v_i}{c}\cos\zeta)}{\sqrt{1 - \left(\frac{v_i}{c}\right)^2}} \tag{A.22}$$

where ζ is the laboratory crossing angle of the photon and ion beams and v_i is the speed of the ion beam. For example, in the case of a 30 keV He^- ion, v_i/c is 0.004. The corresponding first-order Doppler shift is zero for the essentially perpendicular geometry chosen in these experiments. The second order shift is also negligibly small for all beam energies used in this experiment. For the same reasons, the effect of relativity on the value of the crossing angle, as seen from the two frames, is negligible.

The mass of the photodetached electron is much less than the mass of the residual atom for all ions discussed in this thesis. The correction for recoil effects is therefore small, and can be neglected in the kinematic equations.

VITA

Jeffrey Scott Thompson was born in Norman, Oklahoma on May 4, 1960, the son of Elton Ray and Cathren Roselyn Thompson. In 1964, his family moved to Tullahoma, Tennessee where he attended public schools and graduated from Tullahoma High School in June 1978. The following September he entered the University of California, Los Angeles, and in June 1982 he was granted a Bachelor of Science degree in Physics. In the fall of 1982 he accepted a teaching assistantship in the Physics Department at the University of Tennessee and began study toward an advanced degree. He received the Doctor of Philosophy degree with a major in Physics in May 1989. He married Jill Michele Matheson on April 13, 1985.